

## Article

# Development of a 6-DOF Parallel Robot for Potential Single-Incision Laparoscopic Surgery Application <sup>†</sup>

Doina Pisla <sup>1</sup>, Nadim Al Hajjar <sup>2</sup>, Bogdan Gherman <sup>1</sup>, Corina Radu <sup>3</sup>, Tiberiu Antal <sup>1</sup>, Paul Tucan <sup>1,\*</sup>, Ruxanda Literat <sup>1</sup> and Calin Vaida <sup>1,\*</sup>

<sup>1</sup> CESTER, Technical University of Cluj-Napoca, 400114 Cluj-Napoca, Romania

<sup>2</sup> Department of Surgery, "Iuliu Hatieganu" University of Medicine and Pharmacy, 400347 Cluj-Napoca, Romania

<sup>3</sup> Department of Internal Medicine, "Iuliu Hatieganu" University of Medicine and Pharmacy, 400347 Cluj-Napoca, Romania

\* Correspondence: paul.tucan@mep.utcluj.ro (P.T.); calin.vaida@mep.utcluj.ro (C.V.)

<sup>†</sup> This paper is an extended version of the paper published in Pisla, D.; Crisan, N.; Ulinici, I.; Gherman, B.; Radu, C.; Tucan, P.; Vaida, C. Structural Study of a Robotic System for SILS Surgery. In Proceedings of the 8th International Workshop on New Trends in Medical and Service Robotics (MESROB 2023), Craiova, Romania, 7–10 June 2023; pp. 20–31.

**Abstract:** This paper presents the development of a 6-DOF (Degrees of Freedom) parallel robot for single-incision laparoscopic surgery (SILS). The concept of the robotic system is developed with respect to a medical protocol designed by the medical experts in the team targeting a SILS procedure in urology. The kinematic model of the robotic system was defined to determine the singularities that may occur during functioning. FEM analyses were performed to determine the components of the robotic structure that may compromise the rigidity of the robotic system, and these components were redesigned and integrated into the final design of the robot. To verify the kinematic model a series of numerical and graphical simulations were performed, while to test the functionality of the robotic system, a low-cost experimental model was developed. The accuracy of the experimental model was measured using an optical motion tracking system.

**Keywords:** parallel robot; surgical robot; singularity; functional design; FEM



**Citation:** Pisla, D.; Hajjar, N.A.; Gherman, B.; Radu, C.; Antal, T.; Tucan, P.; Literat, R.; Vaida, C. Development of a 6-DOF Parallel Robot for Potential Single-Incision Laparoscopic Surgery Application. *Machines* **2023**, *11*, 978. <https://doi.org/10.3390/machines11100978>

Academic Editor: Dan Zhang

Received: 13 September 2023

Revised: 17 October 2023

Accepted: 20 October 2023

Published: 23 October 2023



**Copyright:** © 2023 by the authors. Licensee MDPI, Basel, Switzerland. This article is an open access article distributed under the terms and conditions of the Creative Commons Attribution (CC BY) license (<https://creativecommons.org/licenses/by/4.0/>).

## 1. Introduction

Surgical techniques underwent several changes over the past few decades with the main advancements in the development of less invasive techniques. Minimally invasive surgery (MIS) became an alternative to conventional surgery approaches due to its advantages (reduced scars after the procedure, reduced trauma of the healthy tissue, reduced loss of blood, and reduced recovery times and hospitalization) [1]. With respect to conventional surgery, the MIS is performed using a reduced number of small incisions, and the operatory field is visualized using 2D or 3D endoscopic cameras. A step forward following the MIS procedures is given by single incision laparoscopic surgery or SILS [2]. SILS uses a single incision or entry point to access the operatory field, having a diameter of 2.5 to 3 cm. The entry point is usually covered using a trocar that allows easy insertion of the instruments without damaging the tissue around the incision or creating any supplementary load over the incision that could lead to tissue rupture. Although the outcomes of the SILS are similar to the MIS, from a medical point of view, the healthy tissue damaged during the SILS procedure is considerably reduced (than MIS), and the healing of the surgery scars has a better cosmesis [3]. There are some challenges when performing SILS, the main challenge being represented by the difficulty of manipulating the medical instruments in the limited workspace given by the single incision. During SILS, the instruments required by this type of procedure are manipulated in such a manner that their paths intersect with each other resulting in mirrored manipulation from the surgeon's perspective. To enhance the SILS

ergonomics, medical instruments have been developed to improve access to the surgical field; hence, there are several types of medical instruments used in SILS that have curved, foldable, or irregular shapes [4]. Due to reduced ergonomics and workspace of the medical instruments, robotic solutions started to be implemented in minimally invasive surgery to efficiently reduce the collisions between the instruments and increase access to the surgical field [5–18]. Several important advancements have been recorded regarding the robotic solution for medical applications. Russel Taylor’s work evolved around enhancing surgical precision and control through the development of robotic systems. His innovations have played a crucial role in revolutionizing minimally invasive procedures improving patient outcomes and expanding the possibilities for robotic healthcare [19–21]. Nabil Simaan’s work revolved around developing snake-like robots and flexible instruments for minimally invasive surgery enabling surgeons to perform complex procedures with enhanced dexterity and precision, contributing to creating a safer environment for human-robot physical interaction [22–24]. Paolo Dario’s research provided insights into bio-inspired robots, characterized by the development of nature-inspired robots, mimicking biological systems for various applications [25–27].

The functional design of minimally invasive robots is a critical aspect of their development to ensure that they can perform complex tasks with accuracy and safety within the confined workspace. Wei et al. [28] presented the structural design of a laparoscopic robot system based on the spherical magnetic field. The authors used mathematical modeling and force/torque analysis to determine the correlation between the inputs of the driving system and the deflection angle of the laparoscopic robot. Tian et al. [29] propose a laparoscopic surgical robot using a design based on axiomatic design theory to make correct decisions in the design process of the robot.

The number of robotic devices for minimally invasive surgery is relatively low, and currently, there are no commercial solutions, especially those developed for SILS. Hence, this paper proposes an innovative 6-DOF parallel robot able to position and orient a mobile platform equipped with surgical instruments for SILS.

Within this paper, after defining the design concept of the parallel robot with respect to the medical protocol for the urology SILS procedure designed by the medical experts in the team, several analyses are performed. First, using the kinematic model of the parallel robot, the singularities are identified, and avoiding intervals for each singularity are defined, also the workspace of the mobile platform guiding the SILS instruments is defined aiming to determine the limitation of the robot. A functional design analysis is carried on to determine the point of the robotic structure where it may become unstable, for which Finite Element Method (FEM) is used. These analyses are performed aiming to define a rigid robotic structure able to provide a safe environment for the patient and for the operator during the medical procedure and at the same time to develop a stable control system able to avoid singularities and perform the surgical task as safely as possible. Numerical and graphical simulations are performed and compared one against the other to validate the kinematic model of the robotic structure. In the end, the experimental model is presented, and several experimental tests are performed to validate the functionality of the prototype and to determine its accuracy.

The paper is structured as follows: Section 2 contains data regarding the medical protocol for SILS and the kinematics of the robotic system for SILS. Section 3 of the paper presents the singularity analysis of the parallel robot and of the mobile platform guiding the SILS instruments and the workspace determination of the mobile platform. Section 4 of the paper presents the design of the robotic system and the design enhancements followed by a numerical and graphical simulation comparison in Section 5. Section 6 describes the development of the experimental model, its functional validation, and the accuracy determination using an optical tracking system. In the end the discussion, conclusions, and references are presented.

## 2. Parallel Robotic System for SILS

### 2.1. Medical Protocol

The SILS robotic system proposed in this paper [30] should comply with the medical protocol of the SILS procedure. In Table 1, the steps of the medical procedure encompassing the medical (non-robotic tasks) and technical (robot-related tasks) ones for each step are presented.

**Table 1.** Medical procedure with robot integration.

Procedural Step	Medical Point-of-View	Robot Point-of-View
Preplanning	✓ Patient condition assessment.	✓ Define the patient's position during the procedure.
	✓ Define the therapeutical approach.	✓ Define the Remote Center of Motion.
Preparation	✓ Place the patient on the operating table	✓ Mount Instruments and a laparoscopic camera
	✓ Make SILS incision.	✓ Test the functionality of the robot
	✓ Insufflate CO <sub>2</sub> in the abdominal cavity.	✓ Place the robot in the home position
Insertion		✓ Position instruments and laparoscope above the Remote Center of Motion
		✓ Insert the instruments and laparoscope in the abdominal cavity
Positioning and Orientation	✓ Monitor the patient's health state	✓ Position the mobile platform around the entry point
		✓ Lock the mobile platform
Surgical Task		✓ Manipulate the surgical instruments and laparoscopic camera with respect to the surgical task
		✓ Remove the instruments and the laparoscope from the abdomen
Procedure ending	✓ Remove CO <sub>2</sub> from the abdominal cavity	✓ Retract mobile platform above the Remote Center of Motion
	✓ Remove SILS port	✓ Position platform in the home Position
	✓ Suture the incision	✓ Remove the instruments and laparoscope

The medical SILS procedure referred to within this paper is renal cyst laparoscopic decortication using the left-side approach. Renal cyst decortication can be performed either through 3–4 cm incisions in the abdomen or through a single intercostal incision. Cyst removal is carried out using specialized instruments, that ideally provide tactile feedback to the surgeon. The procedure does not require the insertion of the surgeon's hand in the abdomen. Furthermore, following the procedure, a small drain is placed inside the patient's body for 1–2 days to drain the kidney area [16,31,32].

### 2.2. The SILS Robot System

Figure 1 presents the kinematic scheme of the parallel robotic system. For the medical procedure, the initial action involves defining the Remote Center of Motion (RCM) [33], which represents the point at the level of the incision through which an instrument/laparoscope is inserted. Patient position, SILS port, and mobile platform's end-effector determine RCM. The laparoscopic camera's tip aligns with the entry point, representing the RCM for the procedure, with instruments having relative RCMs.

The parallel robot is composed of 6 active joints ( $C_{J1}$ ,  $C_{J2}$  and  $C_{J3}$ —cylindrical joints with free rotation,  $T_{J1}$ ,  $T_{J2}$  and  $T_{J3}$ —prismatic joints) and 11 passive joints ( $R_1$ ,  $R_2$ ,  $R_3$ ,  $R_4$ ,  $R_5$ ,  $R_6$ —revolute joints,  $T_1$ —prismatic joint,  $S_{J1}$ ,  $S_{J2}$  and  $S_{J3}$ —spherical joints and  $U_1$ —universal joint). The reference coordinate system for the structure named OXYZ is in the plane defined by the free rotation prismatic joints  $C_{Ji}$  ( $i = 1 \dots 3$ ) and the simple prismatic joints  $T_{Ji}$ , ( $i = 1 \dots 3$ ).

The coordinate system is located on an axis parallel with the axis of translation for the  $C_{Ji}$  ( $i = 1 \dots 2$ ) joints and lies at the lower limit of the  $C_{J2}$  vertical axis. The OX axis's positive direction is in the direction opposite to the  $T_{Ji}$  prismatic joints and the mobile platform;

the OY axis's positive is towards the axis of  $C_{J3}$  and the OZ axis's positive is up along the  $C_{Ji}$  ( $i = 1 \dots 2$ ) axis.

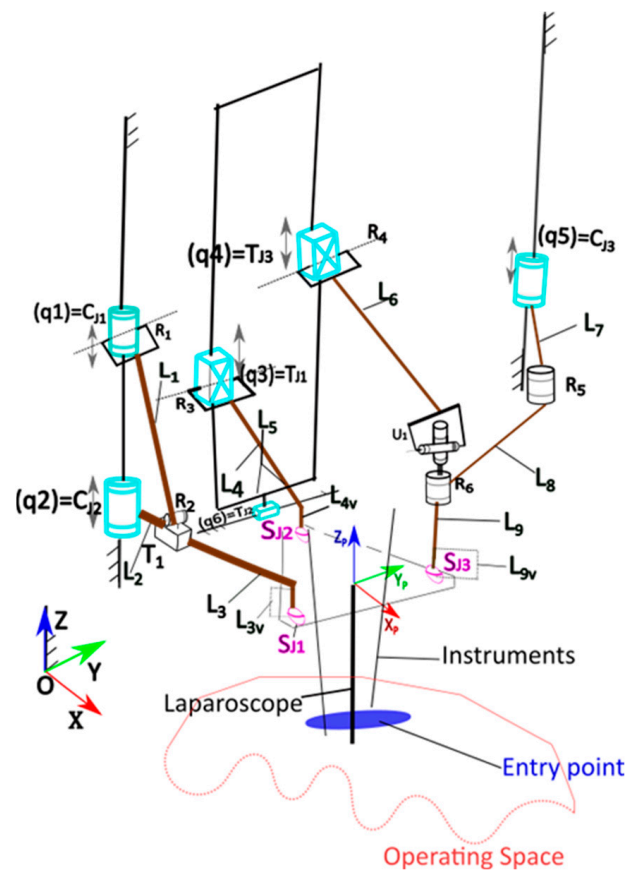


Figure 1. Kinematic scheme of the robotic platform.

The  $O_p X_p Y_p Z_p$  coordinate system which is used to define the kinematics of the mobile platform has been considered to be located at the intersection point of the platform plane and the laparoscopic camera, and can also be defined as the equilateral triangle's (which represents the platform structure) height intersection; it is defined by the  $S_{Ji}$  ( $i = 1 \dots 3$ ) center points.

The kinematics of the robotic system are presented in the following lines using the kinematic scheme from Figure 2 and the geometric parameters defined below:

- $l_{cam}$  is laparoscope length;
- $l_p$  is the distance between the centers of two spherical joints on the mobile platform;
- $h_p$  is the mobile platform's height, defined by spherical joint centers;
- $L_1$  is length  $C_{J1}-T_1$ ;
- $L_2$  is length  $C_{J2}-T_1$ ;
- $L_3$  is length  $T_1-S_{J1}$ ;
- $L_{3v}$  is length  $S_{J1}$  to  $L_3$ ;
- $L_4$  is length  $T_{J1}-S_{J2}$ ;
- $L_{4v}$  is length  $S_{J2}-L_4$ ;
- $L_5$  is length  $T_{J1}-T_{J3}$ ;
- $L_6$  is length  $T_{J3}-U_1$ ;
- $L_7$  is length  $C_{J3}-R_5$ ;
- $L_8$  is length  $R_5-R_6$ ;
- $d_c$  is length  $R_6-U_1$ ;
- $L_9$  is length  $R_6-S_{J3}$ ;
- $L_{9v}$  is length  $S_{J3}-L_9$ .

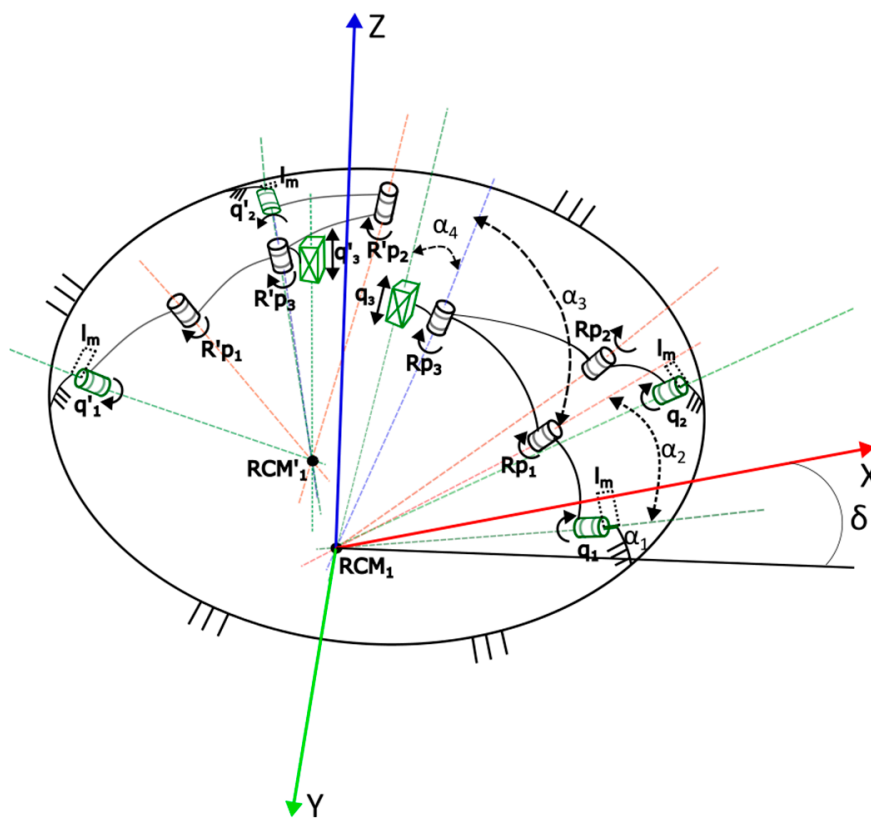


Figure 2. The mobile platform kinematic scheme.

The expression of the active joints of the parallel robot is given in Equation (1)

$$\begin{cases} q_1 = \sqrt{L_1^2 - \left(\sqrt{X_{S1}^2 + Y_{S1}^2} - L_3 - L_{R1} + L_{R2}\right)^2} + q_2 \\ q_2 = Z_{S1} + L_{3v} \\ q_3 = Z_{S2} + \sqrt{L_4^2 - X_{S2}^2} \\ q_4 = Y_P - \frac{2}{3} \cdot h_P \cdot (\sin \psi \cdot \sin \theta \cdot \cos \varphi + \cos \psi \cdot \sin \varphi) - l_{cam} \cdot \sin \psi \cdot \cos \theta \\ q_5 = Z_{S3} + d_c + \sqrt{L_6^2 - X_{Rp6}^2} \\ q_6 = Z_{S3} + L_{9v} \end{cases} \quad (1)$$

where

$$\begin{cases} X_{S1} = X_P + \frac{1}{3} \cdot h_P \cdot \cos \theta \cdot \cos \varphi + \frac{1}{2} \cdot l_P \cdot \cos \theta \cdot \sin \varphi + l_{cam} \cdot \sin \theta \\ Y_{S1} = Y_P + \frac{1}{3} \cdot h_P \cdot (\sin \psi \cdot \sin \theta \cdot \cos \varphi + \cos \psi \cdot \sin \varphi) - \frac{1}{2} \cdot l_P \cdot (-\sin \psi \cdot \sin \theta \cdot \sin \varphi + \cos \psi \cdot \cos \varphi) - l_{cam} \cdot \sin \psi \cdot \cos \theta \\ Z_{S1} = Z_P + \frac{1}{3} \cdot h_P \cdot (-\cos \psi \cdot \sin \theta \cdot \cos \varphi + \sin \psi \cdot \sin \varphi) - \frac{1}{2} \cdot l_P \cdot (\cos \psi \cdot \sin \theta \cdot \sin \varphi + \sin \psi \cdot \cos \varphi) + l_{cam} \cdot \cos \psi \cdot \cos \theta \end{cases} \quad (2)$$

$$\begin{cases} X_{S2} = X_P - \frac{2}{3} \cdot h_P \cdot \cos \theta \cdot \cos \varphi + l_{cam} \cdot \sin \theta \\ Y_{S2} = Y_P - \frac{2}{3} \cdot h_P \cdot (\sin \psi \cdot \sin \theta \cdot \cos \varphi + \cos \psi \cdot \sin \varphi) - l_{cam} \cdot \sin \psi \cdot \cos \theta \\ Z_{S2} = Z_P - \frac{2}{3} \cdot h_P \cdot (-\cos \psi \cdot \sin \theta \cdot \cos \varphi + \sin \psi \cdot \sin \varphi) - l_{cam} \cdot \sin \psi \cdot \cos \theta \end{cases} \quad (3)$$

$$\begin{cases} X_{S3} = X_P + \frac{1}{3} \cdot h_P \cdot \cos \theta \cdot \cos \varphi - \frac{1}{2} \cdot l_P \cdot \cos \theta \cdot \sin \varphi + l_{cam} \cdot \sin \theta \\ Y_{S3} = Y_P + \frac{1}{3} \cdot h_P \cdot (\sin \psi \cdot \sin \theta \cdot \cos \varphi + \cos \psi \cdot \sin \varphi) - \frac{1}{2} \cdot l_P \cdot (-\sin \psi \cdot \sin \theta \cdot \sin \varphi + \cos \psi \cdot \cos \varphi) - l_{cam} \cdot \sin \psi \cdot \cos \theta \\ Z_{S3} = Z_P + \frac{1}{3} \cdot h_P \cdot (-\cos \psi \cdot \sin \theta \cdot \cos \varphi + \sin \psi \cdot \sin \varphi) - \frac{1}{2} \cdot l_P \cdot (\cos \psi \cdot \sin \theta \cdot \sin \varphi + \sin \psi \cdot \cos \varphi) + l_{cam} \cdot \cos \psi \cdot \cos \theta \end{cases} \quad (4)$$

$$\begin{cases} X_{Rp6} = X_{S3} - \sqrt{L_9^2 - (Y_{Rp6} - Y_{S3})^2} \\ Y_{Rp6} = q_4 + \frac{L_5}{2} \end{cases} \quad (5)$$

The implicit functions for the kinematic modeling of the robot are presented below:

$$\left\{ \begin{array}{l} f_1 : q_2 - L_{3v} - Z_{S3} = 0 \\ f_2 : q_1 - q_2 - \sqrt{\left(L_1^2 - \sqrt{X_{S1}^2 - Y_{S1}^2} - L_3\right)^2} = 0 \\ f_3 : q_3 - L_{4v} + Z_{S2} + \sqrt{\left(L_4^2 - X_{S2}\right)^2} = 0 \\ f_4 : q_4 - Y_{S2} - \frac{1}{2}L_5 = 0 \\ f_5 : q_5 - \left[Z_{S3} + d_c + \left(\sqrt{L_6^2 - X_{S3}} - \sqrt{L_9^2 - \left(q_4 + \frac{1}{2}L_5 - Y_{S3}\right)^2}\right)^2\right] = 0 \\ f_6 : q_6 - L_{9v} - Z_{S3} = 0 \end{array} \right. \quad (6)$$

The mobile platform’s role in the surgical procedure and as part of the parallel robotic system is to handle the orientation of the surgical instruments. This is performed by manipulating the instruments with regard to the position and orientation of the instrument tips. In doing this, the platform must respect the RCM of each instrument while avoiding collisions between the instruments and the laparoscopic camera whose position is generally in between the two instruments.

The mobile platform (Figure 3) containing the SILS instruments consists of a circular frame of 600 mm diameter, which is connected to the robot through three points, each one positioned at 120 degrees from the other along the circular frame rim. The platform hosts two 2-DOF parallel spherical mechanisms of type 2-RRR designed to guide each SILS active instrument. The motors, whose shafts are connected to the  $q_1, q_2,$  and  $q_1, q_2,$  active joints, are mounted at an angle  $\alpha_1$  relative to the horizontal plane. This ensures that the axis of the active rotation joints coincides with the RCM point of its respective instrument.

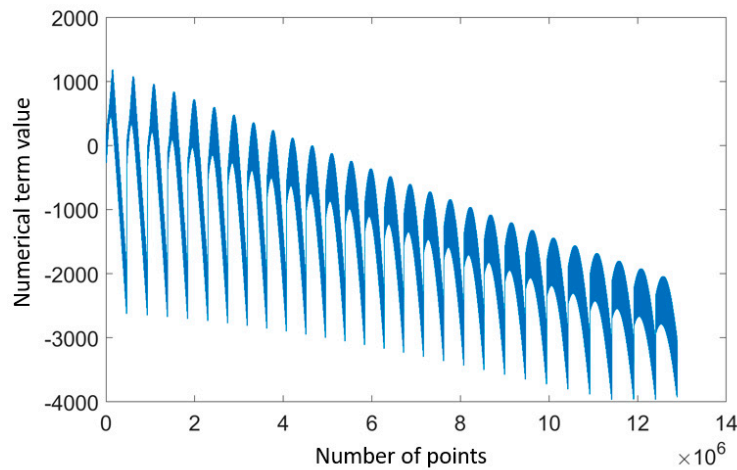


Figure 3. Numerical evaluation of the term  $T_2$ .

In Figure 2, within the first kinematic chain, the  $q_1$  active joint is positioned at an angle  $\alpha_1$  relative to the XOY plane keeping the joint rotation axis colinear with the instrument RCM point. Next,  $q_1$  is connected to a passive revolute joint  $R_{p1}$ , to the second chain.  $R_{p3}$  is connected to  $R_{p1}$  and  $R_{p2}$  through a circular link, constraining their position through the angle  $\alpha_3$ . The situation is similar for the other kinematic chain which consists of the  $q_2$  active joint and the passive revolute joints  $R_{p2}$  and  $R_{p3}$ . The prismatic active joint  $q_3$  is introduced to perform the motion of the active instrument along its vertical axis. This axis is also colinear with the instrument RCM and stands mounted at the angle  $\alpha_4$  from  $R_{p3}$ . During motion, the values of the  $\alpha$  angles can vary, which determines the orientation of the instrument axis.

The kinematic model for the mobile platform is determined, using the Euler angle Z-Y convention of the rotation matrices defining the orientation of the instrument:

$$R_z = \begin{pmatrix} \cos(\psi) & -\sin(\psi) & 0 \\ \sin(\psi) & \cos(\psi) & 0 \\ 0 & 0 & 1 \end{pmatrix}$$

$$R_y = \begin{pmatrix} \cos(\theta) & 0 & \sin(\theta) \\ 0 & 1 & 0 \\ -\sin(\theta) & 0 & \cos(\theta) \end{pmatrix} \quad (7)$$

The center of the coordinate system used for instrument orientation definition is in this mechanism configuration positioned in the RCM of the instrument (8):

$$R_g = \begin{pmatrix} \cos(\psi) & -\cos(\theta)\sin(\psi) & \sin(\psi)\sin(\theta) \\ \sin(\psi) & \cos(\psi)\cos(\theta) & -\cos(\psi)\sin(\theta) \\ 0 & \sin(\theta) & \cos(\theta) \end{pmatrix} \quad (8)$$

The  $q_3$  translation joint is at the upper limit of its motion, with  $R$  representing the radius of the platform frame (9):

$$X_{q_3} = \begin{pmatrix} -R \cdot \sin(\psi) \cdot \sin(\theta) \\ R \cdot \cos(\psi) \cdot \sin(\theta) \\ -R \cdot \cos(\theta) \end{pmatrix} \quad (9)$$

The orientation of the instrument with respect to the  $\alpha_4$  angle is presented in (10):

$$R_{y_{\alpha_4}} = \begin{pmatrix} \cos(\alpha_4) & 0 & -\sin(\alpha_4) \\ 0 & 1 & 0 \\ \sin(\alpha_4) & 0 & \cos(\alpha_4) \end{pmatrix} \quad (10)$$

The RCM coordinate is

$$R_{g_{\alpha_4}} = R_g \cdot R_{y_{\alpha_4}} \quad (11)$$

It is necessary to define the alignment of the  $\beta$  angle which represents the angle between the instrument axis and the  $q_3$  axis, and is also dependent on the  $\alpha_4$  angle:

$$R_{z_{\beta}} = \begin{pmatrix} \cos(\beta) & \sin(\beta) & 0 \\ -\sin(\beta) & \cos(\beta) & 0 \\ 0 & 0 & 1 \end{pmatrix} \quad (12)$$

The RCM coordinate in this case is

$$R_{g_{\beta}} = R_{g_{\alpha_4}} \cdot R_{z_{\beta}} \quad (13)$$

The rotation matrix with respect to the  $\alpha_3$  angle is

$$R_{y_{\alpha_3}} = \begin{pmatrix} \cos(\alpha_3) & 0 & -\sin(\alpha_3) \\ 0 & 1 & 0 \\ \sin(\alpha_3) & 0 & \cos(\alpha_3) \end{pmatrix} \quad (14)$$

The RCM coordinate is

$$R_{g_{\alpha_3}} = R_{g_{\beta}} \cdot R_{y_{\alpha_3}} \quad (15)$$

The rotation of the  $\delta$  angle is defined by the following rotation matrix (16):

$$R_{z_{\delta q_1}} = \begin{pmatrix} \cos(\delta) & \sin(\delta) & 0 \\ -\sin(\delta) & \cos(\delta) & 0 \\ 0 & 0 & 1 \end{pmatrix} \quad (16)$$

The value of  $\alpha_1$  varies by  $-\pi/2$ , executing a rotation around the OY axis, yielding

$$Ry_{\pi/2} = \begin{pmatrix} \cos(\alpha_1 - \frac{\pi}{2}) & 0 & \sin(\alpha_1 - \frac{\pi}{2}) \\ 0 & 1 & 0 \\ -\sin(\alpha_1 - \frac{\pi}{2}) & 0 & \cos(\alpha_1 - \frac{\pi}{2}) \end{pmatrix} \quad (17)$$

and resulting in the position of  $q_1$  (18):

$$Rpoz_{q1} = Rz_{\delta q_1} \cdot Ry_{\pi/2} \quad (18)$$

The definition of the  $q_1$  rotation around OZ is defined as (19)

$$Rz_{q1} = \begin{pmatrix} \cos(q_1) & -\sin(q_1) & 0 \\ \sin(q_1) & \cos(q_1) & 0 \\ 0 & 0 & 1 \end{pmatrix} \quad (19)$$

The position of  $q_1$  is

$$Rpoz_{q1} = Rpoz_{q1} \cdot Rz_{q1} \quad (20)$$

The equation defining the position of  $q_1$  is (21)

$$\sin(\alpha_3) \cdot (\sin(\beta) \cdot \sin(\theta) - \cos(\beta) \cdot \sin(\alpha_4) \cdot \cos(\theta)) - \cos(\alpha_2) \cdot \cos(\alpha_1 - \frac{\pi}{2}) + \cos(\alpha_3) \cdot \cos(\alpha_4) \cdot \cos(\theta) - \cos(q_1) \cdot \sin(\alpha_2) \cdot \sin(\alpha_1 - \frac{\pi}{2}) = 0 \quad (21)$$

From (21) results the double solution for the X-Z coordinates of  $q_1$  (22):

$$q_{1\_1} = -\arccos\left(\frac{\sin(\alpha_3) \cdot (\sin(\beta) \cdot \sin(\theta) - \cos(\beta) \cdot \sin(\alpha_4) \cdot \cos(\theta)) - \cos(\alpha_2) \cdot \sin(\alpha_1) + \cos(\alpha_3) \cdot \cos(\alpha_4) \cdot \cos(\theta)}{-\sin(\alpha_2) \cdot \cos(\alpha_1)}\right) \quad (22)$$

$$q_{1\_2} = \arccos\left(\frac{\sin(\alpha_3) \cdot (\sin(\beta) \cdot \sin(\theta) - \cos(\beta) \cdot \sin(\alpha_4) \cdot \cos(\theta)) - \cos(\alpha_2) \cdot \sin(\alpha_1) + \cos(\alpha_3) \cdot \cos(\alpha_4) \cdot \cos(\theta)}{-\sin(\alpha_2) \cdot \cos(\alpha_1)}\right)$$

The definition of the  $q_2$  equations, for the second kinematic chain involved in the instrument's orientation mechanism, is defined in the following equation. Firstly, the rotation of the  $\delta$  angle with regard to the OZ axis is defined (23):

$$Rz_{\delta q_2} = \begin{pmatrix} \cos(\delta) & -\sin(\delta) & 0 \\ \sin(\delta) & \cos(\delta) & 0 \\ 0 & 0 & 1 \end{pmatrix} \quad (23)$$

The rotation around the OY axis is defined by the value of the  $\alpha_1$  angle in increments of  $\pi/2$  (24):

$$Ry_{\pi/2} = \begin{pmatrix} \cos(\alpha_1 - \frac{\pi}{2}) & 0 & \sin(\alpha_1 - \frac{\pi}{2}) \\ 0 & 1 & 0 \\ -\sin(\alpha_1 - \frac{\pi}{2}) & 0 & \cos(\alpha_1 - \frac{\pi}{2}) \end{pmatrix} \quad (24)$$

From (23) and (24) we obtain (25)

$$Rpoz_{q2} = Rz_{\delta q_2} \cdot Ry_{\pi/2} \quad (25)$$

For the definition of the rotation around the OZ axis, the following rotation matrix is defined (26):

$$Rz_{q2} = \begin{pmatrix} \cos(q_2) & -\sin(q_2) & 0 \\ \sin(q_2) & \cos(q_2) & 0 \\ 0 & 0 & 1 \end{pmatrix} \quad (26)$$

The position of  $q_2$  is

$$Rpoz_{q2} = Rpoz_{q2} \cdot Rz_{q2} \quad (27)$$

The rotation around OY by the value of  $\alpha_2$  is obtained by (28)

$$Ry\alpha_2q_2 = \begin{pmatrix} \cos(\alpha_2) & 0 & \sin(\alpha_2) \\ 0 & 1 & 0 \\ -\sin(\alpha_2) & 0 & \cos(\alpha_2) \end{pmatrix} \quad (28)$$

The equation defining the  $q_2$  value after replacement with half angle tangent is (29)

$$\begin{aligned} & (\cos(\psi) \cdot \sin(\alpha_4) - \cos(\alpha_4) \cdot \sin(\psi) \cdot \sin(\theta)) \\ & \cdot \left( \cos(\alpha_1) \cdot \cos(\alpha_2) \cdot \cos(\delta) + \frac{2 \cdot t_2 \cdot \sin(\alpha_2) \cdot \sin(\delta)}{t_2^2 + 1} + \frac{\cos(\delta) \cdot \sin(\alpha_1) \cdot \sin(\alpha_2) \cdot (t_2^2 - 1)}{t_2^2 + 1} \right) - \cos(\alpha_3) + \cos(\alpha_4) \cdot \cos(\theta) \\ & \cdot \left( \cos(\alpha_2) \cdot \sin(\alpha_1) - \frac{\cos(\alpha_1) \cdot \sin(\alpha_2) \cdot (t_2^2 - 1)}{t_2^2 + 1} \right) + (\sin(\alpha_4) \cdot \sin(\psi) + \cos(\alpha_4) \cdot \cos(\psi) \cdot \sin(\theta)) \\ & \cdot \left( \cos(\alpha_1) \cdot \cos(\alpha_2) \cdot \sin(\delta) - \frac{2 \cdot t_2 \cdot \cos(\delta) \cdot \sin(\alpha_2)}{t_2^2 + 1} + \frac{\sin(\alpha_1) \cdot \sin(\alpha_2) \cdot \sin(\delta) \cdot (t_2^2 - 1)}{t_2^2 + 1} \right) = 0 \end{aligned} \quad (29)$$

### 3. Singularity Analysis

The singularity analysis can be performed after proper determination of the kinematic model [34,35]. To determine the singularities of the parallel robot, the determinants of the two Jacobi matrices will be analyzed [36]. It is known from [37,38] that three types of singularities can be defined: type 1 singularity, when the determinant of the Jacobi matrix for the direct model is equal to zero, type 2 singularities, when the determinant of the Jacobi matrix for the inverse model becomes zero, and type 3 singularities, when both determinants vanish at the same time.

The Jacobi matrix for the direct model is given in Equation (30) yielding the value of determinant  $-1$ .

$$B = \begin{pmatrix} 0 & 1 & 0 & 0 & 0 & 0 \\ 1 & -1 & 0 & 0 & 0 & 0 \\ 0 & 0 & 1 & 0 & 0 & 0 \\ 0 & 0 & 0 & 1 & 0 & 0 \\ 0 & 0 & 0 & B_{54} & 1 & 0 \\ 0 & 0 & 0 & 0 & 0 & 1 \end{pmatrix} \quad (30)$$

The determinant of the Jacobi matrix A does not share the same simple expression, and the mathematical computation returned a factored result of the determinant of matrix A containing 9 terms. One way to search for singularities is to analyze every term of this product with respect to zero. However, this is not sufficient, as singularities or abnormal robot behavior can also appear for very small values of the determinant (near singular poses) and this analysis will be conducted numerically for the entire determinant.

The first term of the determinant A is:

$$T_1 = -\frac{3}{4} \quad (31)$$

This term is constant and does not introduce any singularities for the robot.

The  $T_4$  term is

$$T_4 = lp^3 \quad (32)$$

The geometrical interpretation of this term corresponds to the case when all the spherical joints of the robot would superpose, for a platform with the side length equal to zero. This is a purely theoretical situation that will never be encountered by the robot.

The  $T_9$  term is

$$T_9 = \frac{1}{\sqrt{9 \cdot L_4^2 - 9 \cdot X_P^2 + 6 \cdot X_P \cdot l_P \cdot \sqrt{3} \cdot \cos(\varphi) \cdot \cos(\theta) - 3 \cdot l_P^2 \cdot \cos^2(\varphi) \cdot \cos^2(\theta)}} \quad (33)$$

The last expression is a quadratic equation, which can be written as a product of two expressions:

$$EXP = \sqrt{\left(l_p\sqrt{3}\cos(\varphi)\cos(\theta) + 3L_4 - 3X_P\right)\left(-l_p\sqrt{3}\cos(\varphi)\cos(\theta) + 3L_4 + 3X_P\right)} \quad (34)$$

Considering that:  $X_P > 0$  and  $L_P = l_p$ , only the first term must be analyzed, resulting in

$$X_P \leq L_4 + l_p \cdot \frac{\sqrt{3}}{3} \cos(\varphi) \cos(\theta) \quad (35)$$

yielding

$$\cos(\theta) = 0 \Rightarrow \theta = \pm \frac{\pi}{2} \quad (36)$$

This equation illustrates a singularity of the robot when the platform is tilted  $90^\circ$  (the laparoscope in a horizontal position), which is outside the operational workspace of the robot.

The other terms are too long to be represented here as equations, but they are evaluated numerically in MATLAB inside the operational workspace of the robot.

All the terms have been evaluated for the entire operational workspace and tilting angles of

$$\begin{aligned} \psi &\in [-30^\circ \div 30^\circ] \\ \theta &\in [-30^\circ \div 30^\circ] \\ \varphi &\in [-30^\circ \div 30^\circ] \end{aligned} \quad (37)$$

The numerical evaluation revealed values of the term  $T_2$  within the interval from (38). The value of the determinant changes with the increase of the angle  $\psi$ , also reducing the spread between the minimum and maximum values of the term  $T_2$ .

For easier evaluation of the terms a graphical representation is displayed in Figure 3:

$$T_{2\_min} = -3.9665 \cdot 10^3 \text{ and } T_{2\_max} = 1.1871 \cdot 10^3, \min|T_2| = 0.0196 \quad (38)$$

The numerical evaluation revealed values of the term  $T_5$  within the interval shown in Equation (39). The evaluation of term  $T_5$  during the numerical evaluation is presented in Figure 4.

$$T_{5\_min} = 1.9356 \cdot 10^{-4} \text{ and } T_{5\_max} = 0.0777 \quad (39)$$

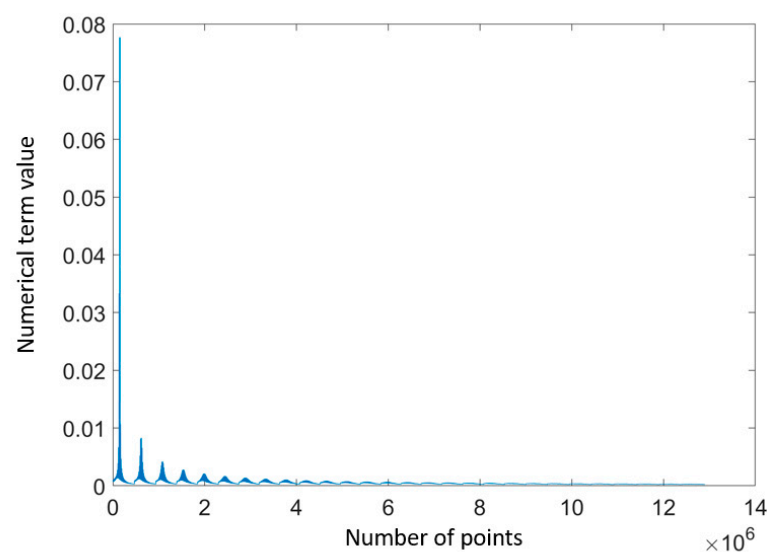


**Figure 4.** Numerical evaluation of the term  $T_5$ .

The numerical evaluation revealed values of the term  $T_6$  within the interval from Equation (40), and the graphical representation is shown in Figure 5.

$$T_{6\_min} = 2.8986 \cdot 10^{-4} \text{ and } T_{6\_max} = 0.0609 \quad (40)$$

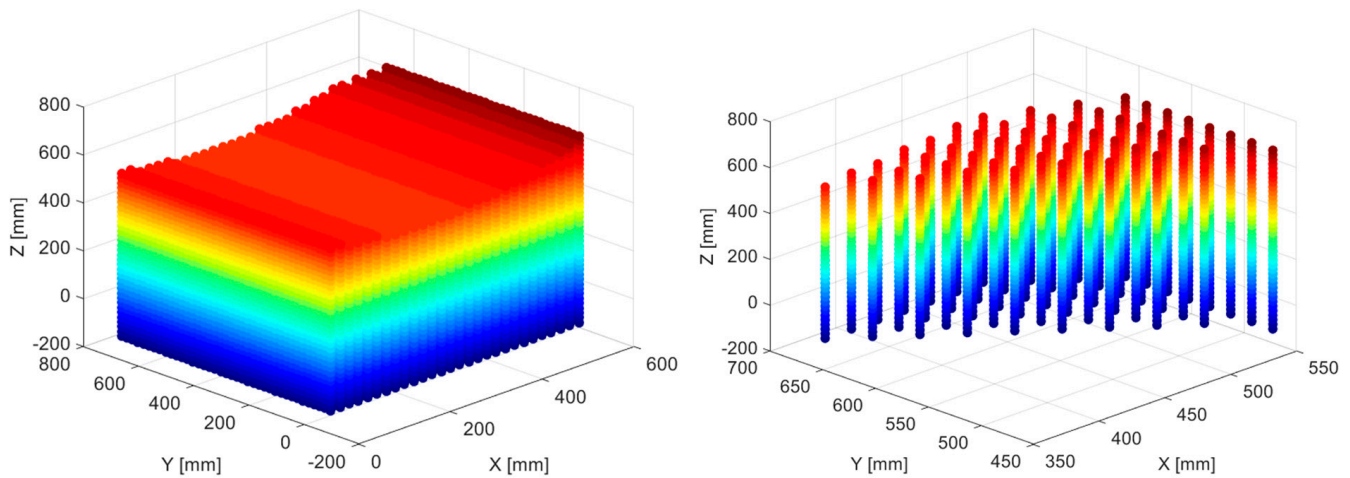


**Figure 5.** Numerical evaluation of the term  $T_6$ .

Even though the term did not reveal any real singular values, the term recorded around 1% of the numerical values as complex numbers, all located in the area displayed on the right side of the figure, an area that should be avoided during the operation of the robot. The left graphic represents the entire end-effector workspace which was used for the evaluation of the determinant while the right side of the figure represents the points that determine complex values for the active joint of the robot. As the complex values do not seem to point towards any specific geometric configurations, after the individual analysis of each factor of the determinant  $A$ , the entire determinant will be assessed numerically for the same workspace to establish whether the points revealed by term  $T_6$  are actual configurations which cannot be reached, or they represent mathematical artifacts caused by the Maple factorization function.

The numerical evaluation revealed values of the term  $T_7$  within the interval from Equation (41), as shown in Figure 6:

$$T_{7\_min} = 5.9255 \cdot 10^{-4} \text{ and } T_{7\_max} = 8.2971 \cdot 10^{-4} \quad (41)$$

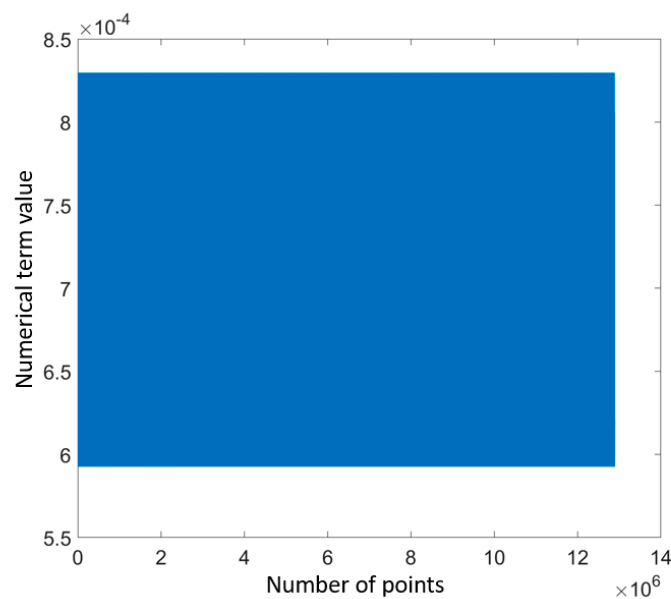


**Figure 6.** Numerical evaluation of the term  $T_7$ .

The numerical evaluation revealed values of the term  $T_8$  within the interval from Equation (42) and graphically represented in Figure 7:

$$T_{8\_min} = 3.3333 \cdot 10^{-4} \text{ and } T_{8\_max} = 7.4647 \cdot 10^{-4} \quad (42)$$

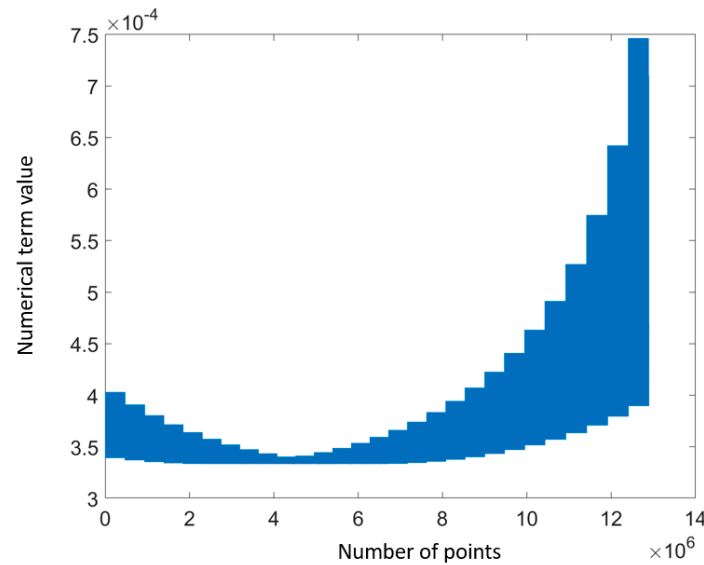


**Figure 7.** Numerical evaluation of the term  $T_8$ .

Due to the behavior of several terms from the factor expression of the determinant  $A$ , a numerical evaluation was performed on the entire determinant using all the points within the robot's operational workspace. As this approach is purely numerical it cannot provide specific information about the geometrical configurations of the robot, but as it can be seen in Figure 8 it also validates the points which the independent evaluation of the term  $T_6$  revealed to have complex solutions for the active joints.

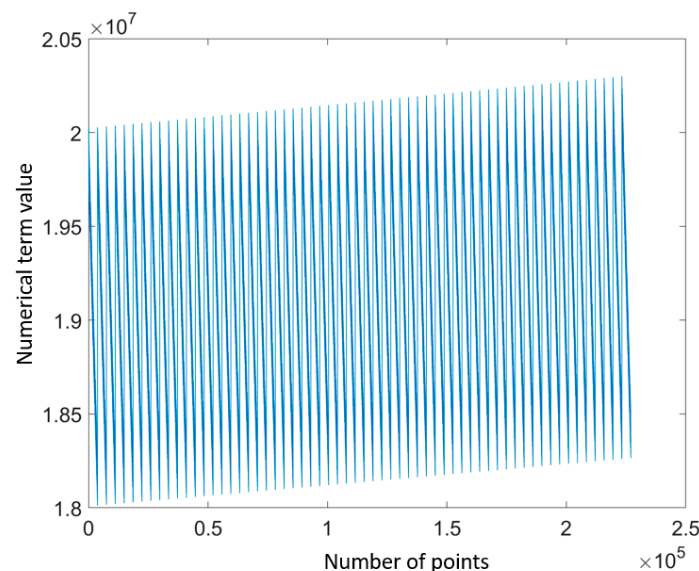


**Figure 8.** Numerical evaluation of the entire determinant in the operational workspace for one point and full orientations.

Even though this approach is not perfect, as there might be specific geometric configurations that could not be identified through this process, based on the values of the determinant inside the operational workspace of the robot, it is safe to assume that there are no singular points inside this volume, validating the robot usage.

A final assessment of the determinant is carried out for the scenario when the endoscopic camera is located inside the patient's body, where the platform will perform only the orientation of the laparoscopic camera (see Figure 9).

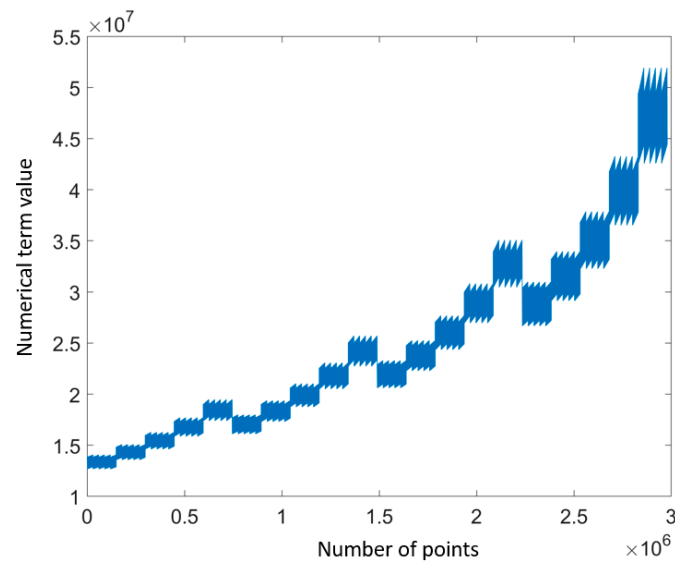


**Figure 9.** Numerical evaluation of the entire determinant in the operational workspace for central points with full orientations.

For the workspace analysis of the instruments guided by the mobile platform, the XOY motion of the instrument tip has been evaluated at various insertion levels, respecting the constraint of the RCM at insertion. Additionally, the workspace of the spherical mechanism located above the RCM has also been evaluated (Figure 10).

#### The SILS instrument orientation mechanism workspace

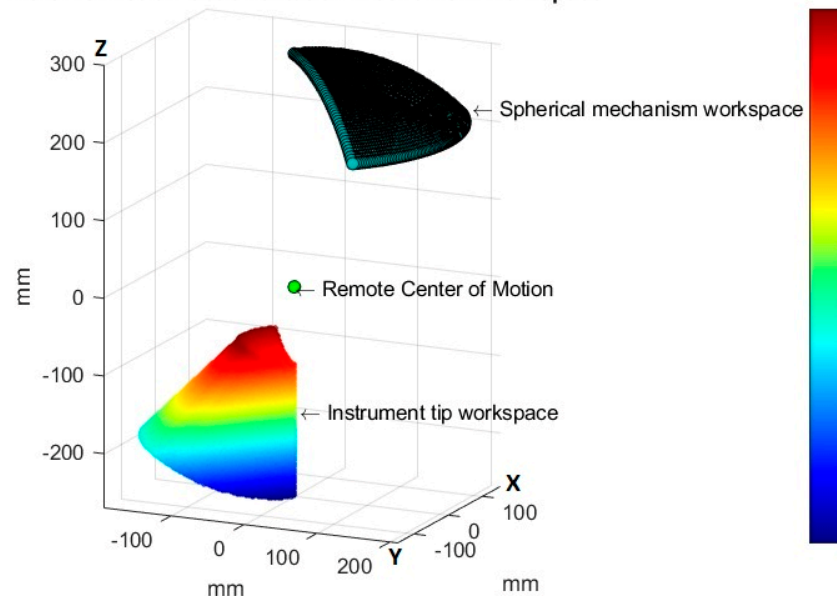


**Figure 10.** Workspace of the mobile platform.

It has been determined that as the insertion of the instrument advances in the operative space, the workspace for the instrument tip increases. As the mechanism that fulfills insertion does not influence the spherical orientation mechanism, the spherical mechanism workspace remains unaltered by instrument insertion depth.

#### 4. The CAD of the Parallel Robot

The SILS parallel robot presented in Figure 11 is composed of two modules: the parallel robot and the mobile platform guiding the SILS instruments. The parallel robot is used in all surgical stages including the docking stage, with a role in the orientation of the laparoscopic instrument during the surgical stage, while also being used for the un-docking of the mobile platform following the completion of the active surgical stage. On the other hand, the mobile platform is only used during the surgical stage for the manipulation of the active surgical instruments.

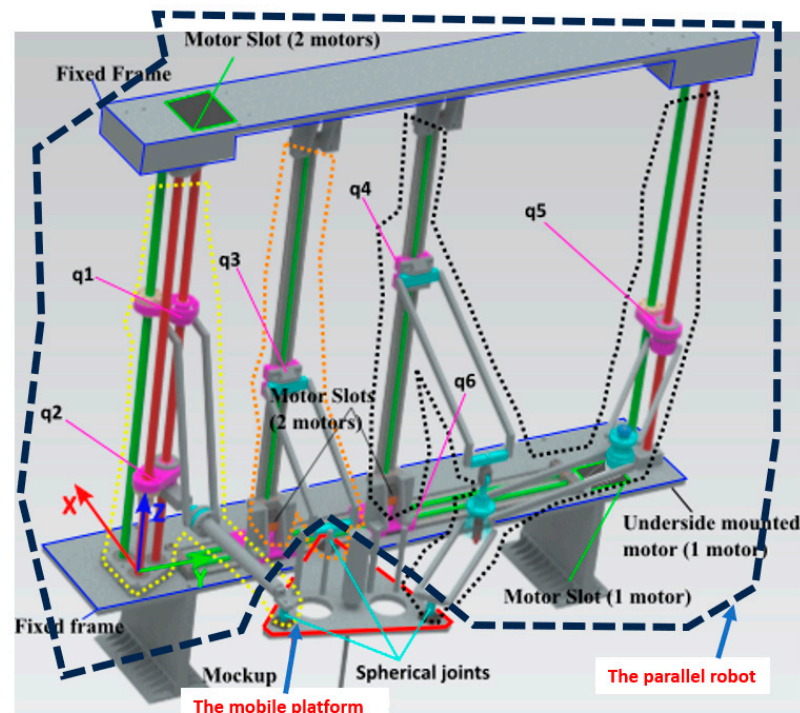


Figure 11. The 3D CAD model of the SILS parallel robot.

The parallel robot has 6 DOF, providing the necessary range of motion for docking, alignment, and laparoscope orientation, executing translations along each of the three motion axes  $X$ ,  $Y$ ,  $Z$ , and rotations around these three axes. The mobile platform can execute independent motions for each of the two active instruments used in the surgical procedure. Each instrument performs a translation along its longitudinal axis ( $Z$  mobile axis) and rotations around the  $X$  and  $Y$  axes. For each instrument, the platform uses a spherical parallel mechanism, allowing a wide workspace for the orientation of the instruments, the finer motions required for actuating the distal head of the surgical instruments being achieved by a separate mechanism located in the instrument's proximal head. Thus, at the level of the entire robot system, the end-effector of the platform is not considered to be the instrument tip, but the complete set of the three instruments (the laparoscopic camera and the two active surgical tools).

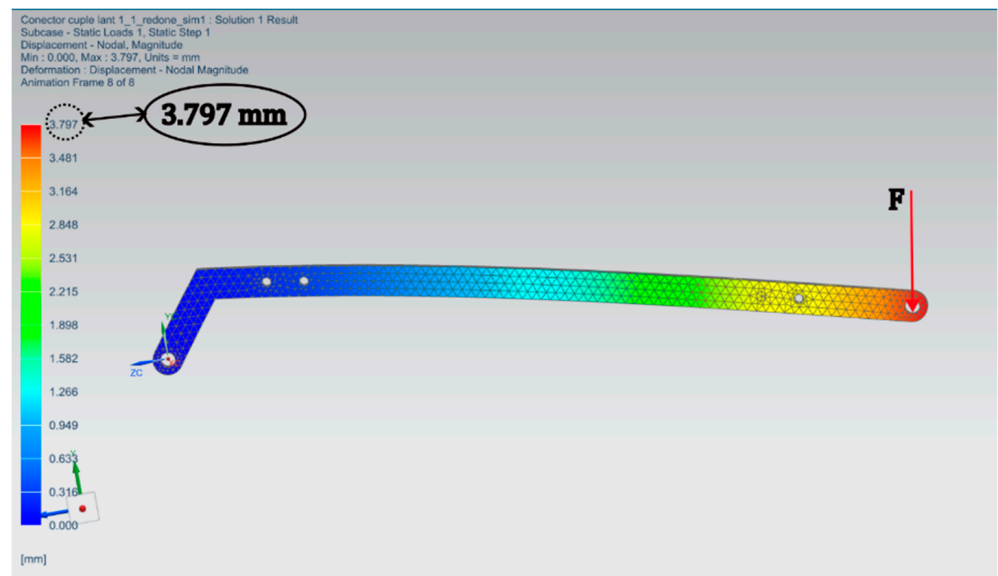
##### *Structural Analysis of the Main Components*

Based on the results of the FEM analyses on the joint connecting links, several mechanical components were redesigned to reduce the nodal displacements. Thus, after the redesign, the components had to be tested again to analyze the displacements during simulation under the same conditions. As a result, the design in Figure 12 was adopted. The new components were tested to determine the displacement values. The components were manufactured using a professional 3D printer using acrylonitrile butadiene styrene (ABS), during the analysis the weight of each component was taken into consideration, and gravitational forces were applied.

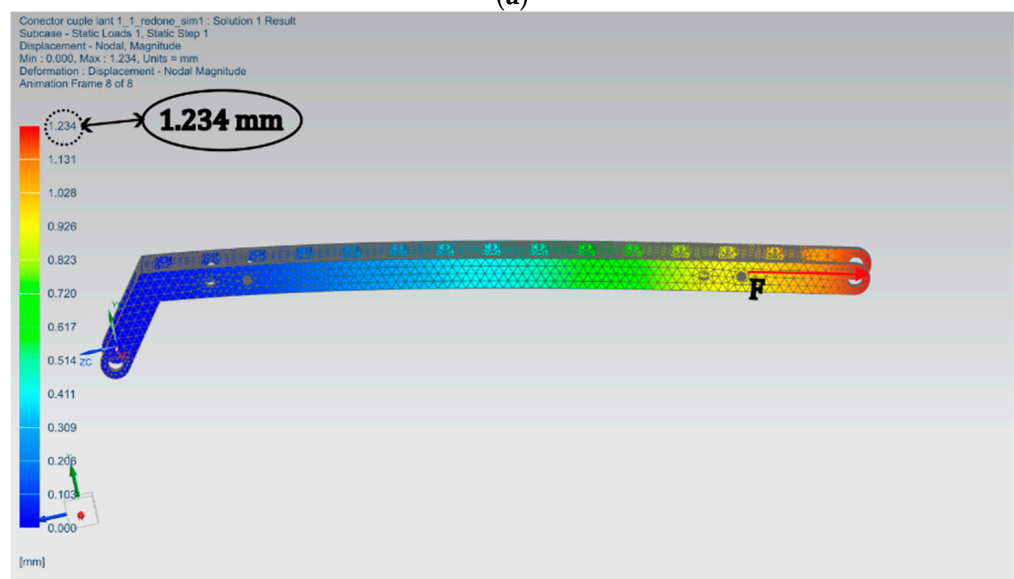


Figure 12. Redesign of connecting links.

In the case of the  $L_1$  link, the redesigned element was placed under a force of  $F = 80$  N in the negative Y (Figure 13a) and negative Z direction (Figure 13b). The results revealed that the new design reduced the overall displacements.



(a)

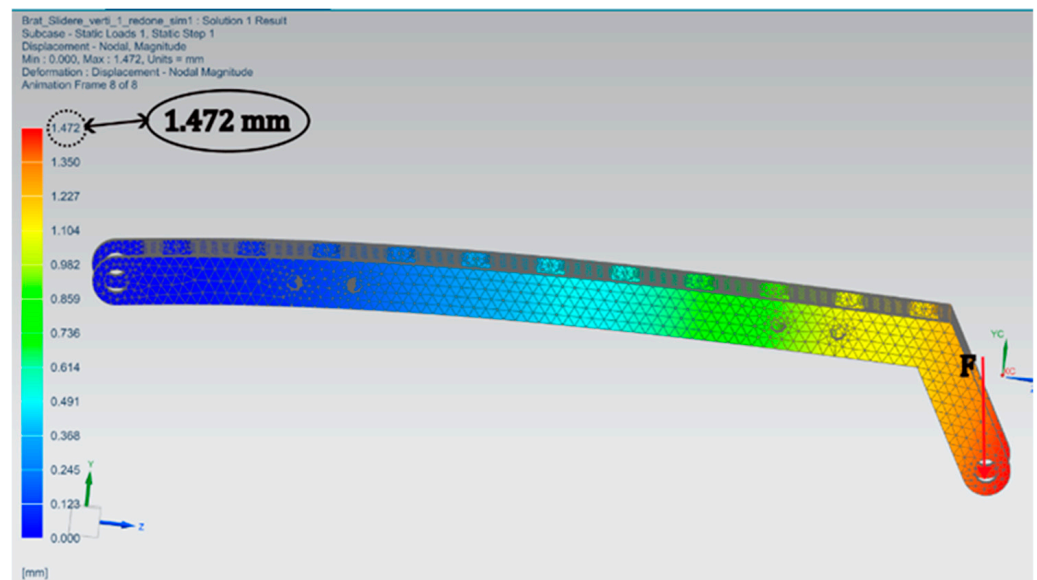


(b)

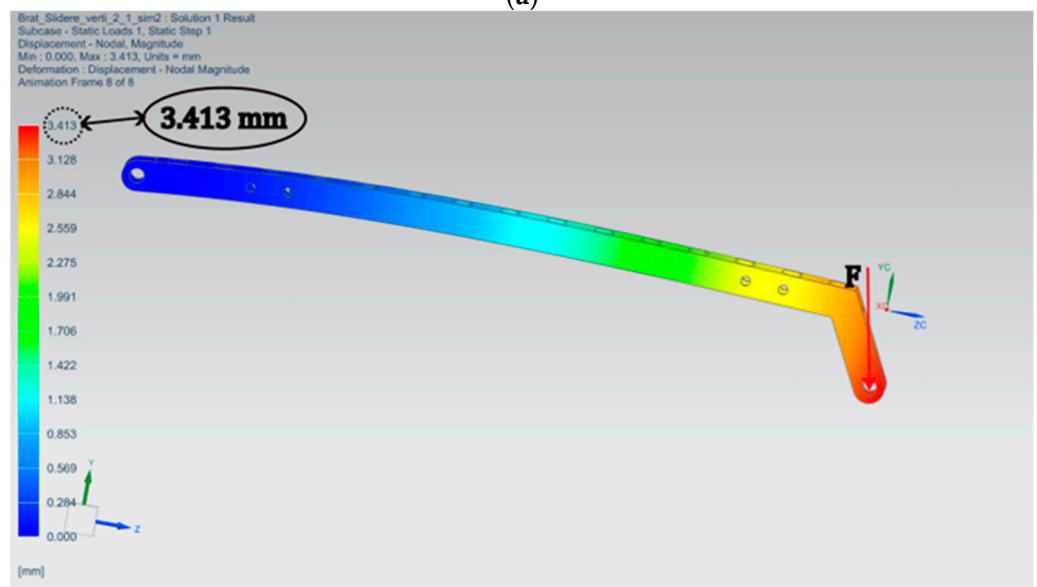
Figure 13. Nodal displacements on link  $L_1$ . (a) Nodal displacement of the  $L_1$  link under force  $F_Y$ ; (b) Nodal displacement of the  $L_1$  link under force  $F_Z$ .

In the case of the negative Y displacement, a reduction of approximately 66% was achieved with the displacement being reduced from 8.538 mm to 3.797 mm. A more significant reduction was observed in the case when the force applied was in the direction of the negative Z axis, from 17.38 mm to 1.234 mm, which represents almost 93%.

In the case of the  $L_4$  link a reduction was also observed (Figure 14a), from 3.272 mm to 1.472 mm, which amounts to 63%. In the case of the  $L_6$  link, the displacement went from 5.960 mm to 3.413 mm, which represents a 43% reduction (Figure 14b).



(a)



(b)

**Figure 14.** Nodal displacements on link  $L_4$ . (a) Nodal displacement of the  $L_4$  link under force  $F_Y$ ; (b) Nodal displacement of the  $L_6$  link under force  $F_Y$ .

In the case of the  $L_7$  link the displacement was reduced from 11.321 mm to 5.172 mm, which is almost 55% (Figure 15a). For the  $L_8$  link (Figure 15b) the maximum displacement was reduced from 8.106 mm to 3.723 mm or a little over 54%. Finally, for the  $L_9$  link a reduction of under 55% from 14.57 mm to 6.561 mm (Figure 15c) was obtained.

Based on the results of the FEM analyses, the new structures were adopted into the development of the robotic device.

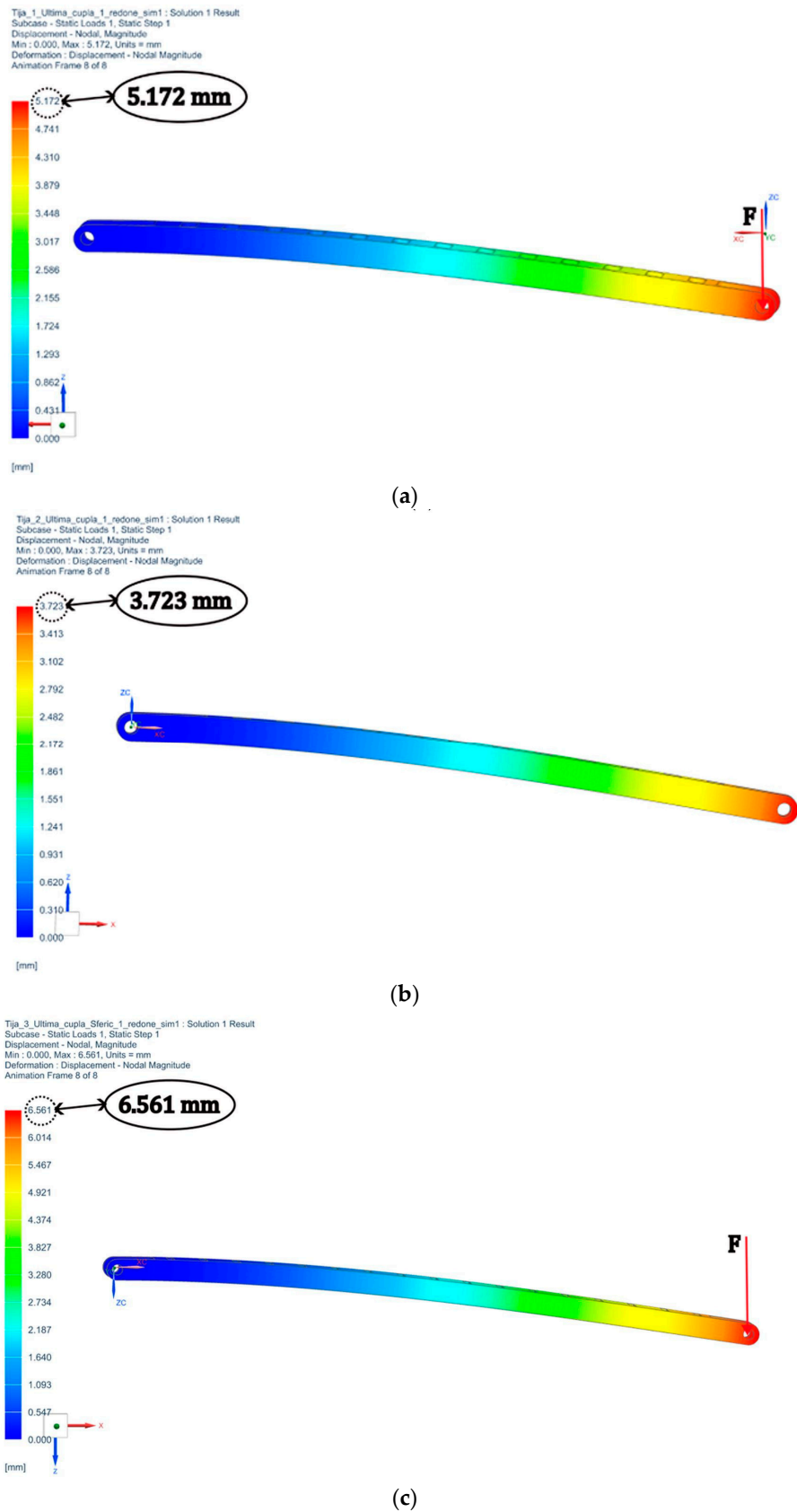


**Figure 15.** Nodal displacements on links  $L_7$ ,  $L_8$ , and  $L_9$ . (a) Nodal displacement of the  $L_7$  link under force  $F_Z$ ; (b) nodal displacement of the  $L_8$  link under force  $F_Z$ ; (c) nodal displacement of the  $L_9$  link under force  $F_Z$ .

### 5. Performed Simulations

To study and validate the kinematic models of the 6-DOF robotic device, a numerical simulation was performed. The numerical model of the robot was analysed and relevant trajectories for the medical act were defined. The following geometrical parameters were used in the simulations:

$$\begin{aligned}
 l_1 &= 575 \text{ mm}; \quad l_3 = 200 \text{ mm}; \quad l_{3v} = 50 \text{ mm}; \quad l_4 = 400 \text{ mm}; \\
 l_5 &= 250 \text{ mm}; \quad l_6 = 500 \text{ mm}; \quad l_7 = 600 \text{ mm}; \quad l_8 = 400 \text{ mm}; \\
 l_9 &= 300 \text{ mm}; \quad l_{9v} = 50 \text{ mm}; \quad dc = 50 \text{ mm}; \quad l_p = 250 \text{ mm}; \quad l_{cam} = 300 \text{ mm}
 \end{aligned}
 \tag{43}$$

The simulation assumes the displacement of the robotic device from an arbitrary point in space to a location (above the patient) to prepare the instrument insertion inside the body, imposing thus the positioning of the laparoscopic camera on a vertical trajectory (parallel with the Oz axis). In this case, the simulation parameters are:

$$\text{Initial pose : } \begin{cases} X_E = 200 \text{ [mm]} \\ Y_E = 200 \text{ [mm]} \\ Z_E = 400 \text{ [mm]} \\ \psi_E = 10 \text{ [deg]} \\ \theta_E = 10 \text{ [deg]} \\ \varphi_E = 0 \text{ [deg]} \end{cases} \Rightarrow \text{Final pose : } \begin{cases} X_E = 250 \text{ [mm]} \\ Y_E = 300 \text{ [mm]} \\ Z_E = 300 \text{ [mm]} \\ \psi_E = 0 \text{ [deg]} \\ \theta_E = 0 \text{ [deg]} \\ \varphi_E = 0 \text{ [deg]} \end{cases}
 \tag{44}$$

For the motion parameters, defined at the level of the laparoscope tip, a maximum velocity of 10 mm/s and a maximum acceleration of 5 mm/s<sup>2</sup> were used.

The numerical simulation using the parameters defined above was performed using MATLAB. In Figure 16, the time-based variation of the displacements (green color), velocities (yellow color), and accelerations (red color) of the end-effector coordinates (the laparoscopic tip) are illustrated, while Figure 17 presents the data corresponding to the motion of the active joints (using the same code of colors). Complementarily, a graphical simulation of the robot, using the same input parameters, was performed using Siemens NX.

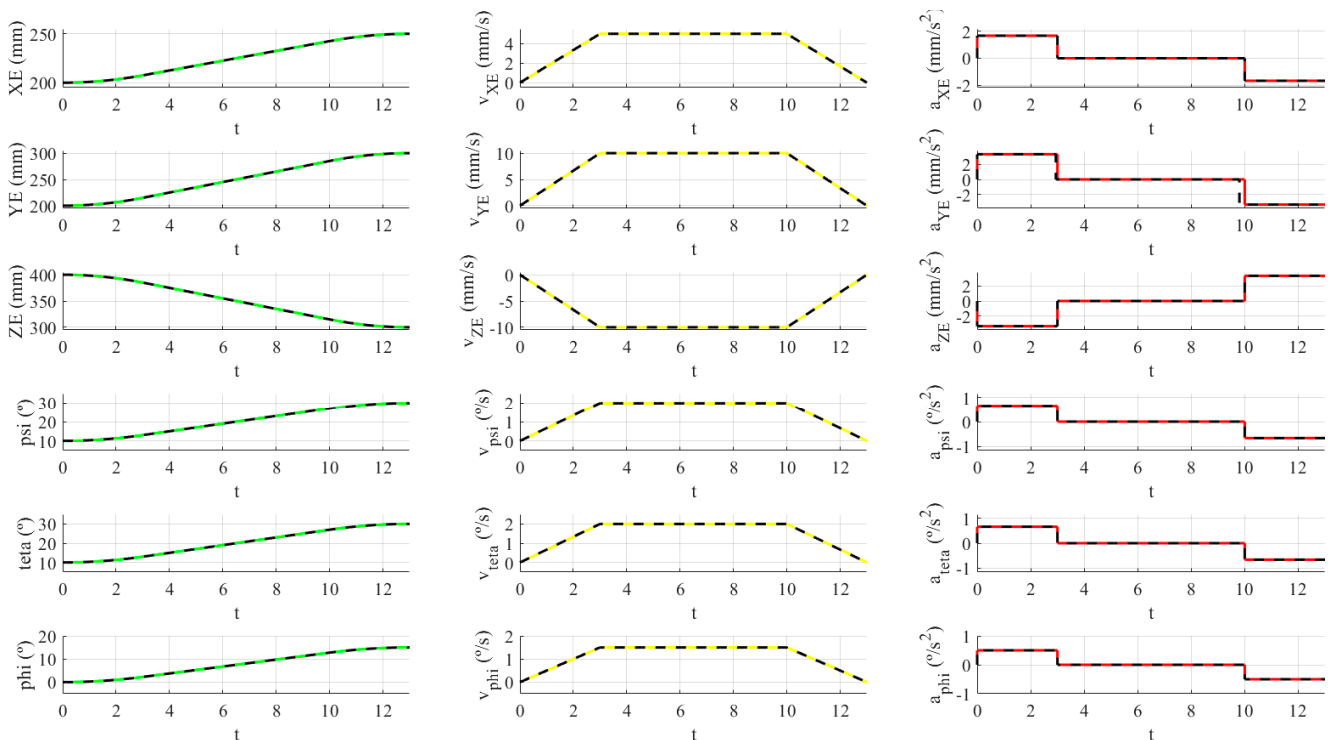
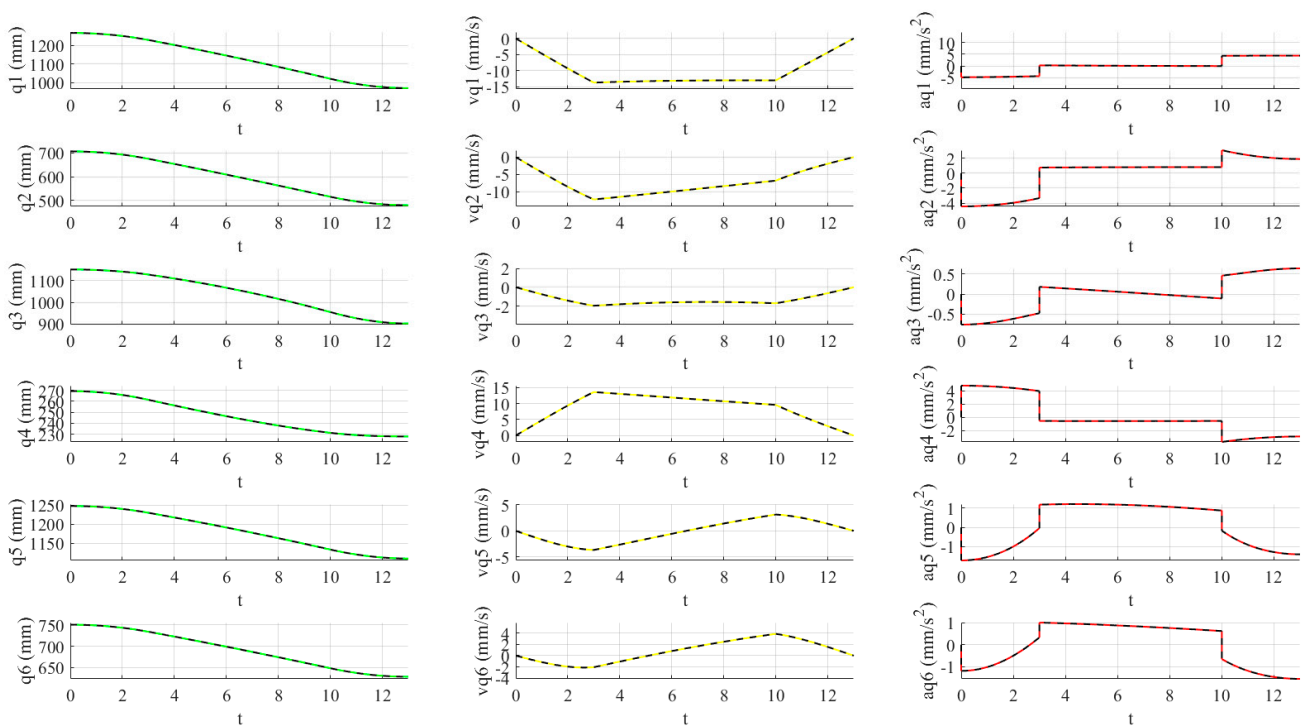


Figure 16. Time history diagram of the coordinates of the laparoscope.



**Figure 17.** Time history diagram of the active joints of the parallel robot.

Data obtained from the graphical simulation was superposed above data obtained from the numerical simulation (black dotted line in Figures 16 and 17). The results of the comparison between the two simulations reveal no differences in terms of position, velocity, and accelerations at the level of the active joints and end-effector, validating the kinematic model of the robot and allowing further development of the robot towards the experimental model.

## 6. Experimental Model and Functional Validation

The experimental model of the parallel robot for SILS is presented in Figure 18.

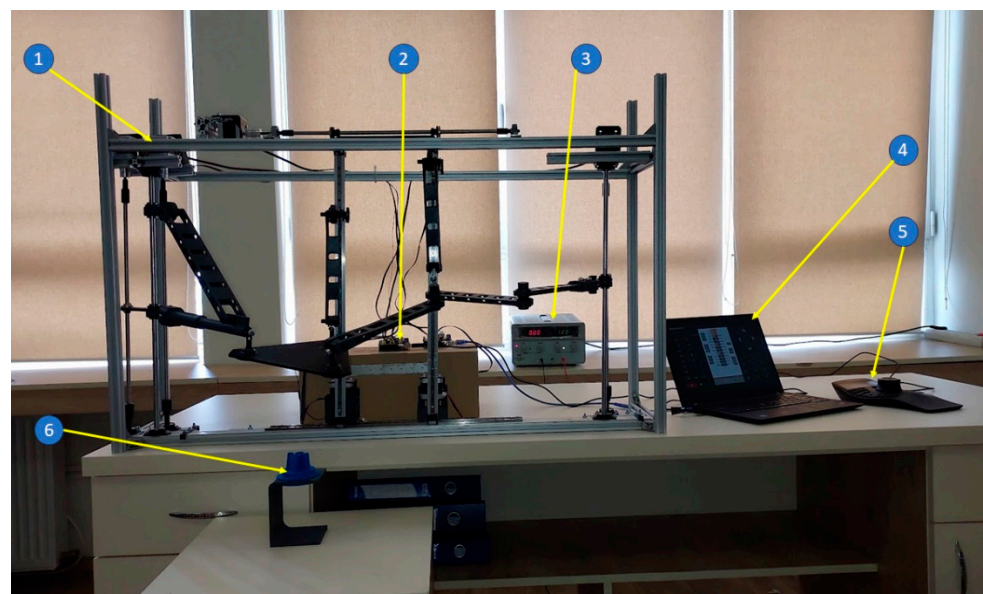


**Figure 18.** Experimental model and functional validation setup.

To test the functionality of the experimental model, a simple experimental test has been designed to demonstrate its ability to position the platform in its required position, to insert the platform within the desired operative space, and orient the platform within that space. The kinematics of the robot detailed in the previous section, the results of the singularity analysis (the avoidance intervals for the nine terms defined above), and the limitations obtained during the workspace analysis were implemented in the control system of the parallel robot.

The main components of the experimental setup are as follows:

1. The SILS parallel robot (composed of a mechanical structure and six stepper motors);
2. The motor drivers;
3. The power supply (12 V);
4. A computer with a simple user interface and control software that integrates the robot kinematic model with the motions of a 3D SpaceMouse;
5. The 3D SpaceMouse (Space explorer from 3DConnection);
6. A SILS port simulator.

To simulate as close as possible the surgical process, a 6-DOF device was used to manipulate the robotic platform, representing one of the possible devices that can be used on a master console.

Using a custom-made Python library, the equations of the robot inverse kinematic model were connected to the motions of the SpaceMouse. Thus, by moving the knob, the user issues incremental motion commands to the robot as simple translations or rotations, or any combination of the above, enabling the input of any trajectory using visual feedback (like the Master console of a surgical robot).

Several tests were performed (Figures 19–22):

1. The motion of the robot within its operational workspace (to simulate the motion of the robot from an arbitrary position to the location of the SILS port);
2. The insertion of the simulated instrument into the SILS port, which was attached to a 3D printed support;
3. The motion of the instrument after its insertion respects the constraint of the entry port (the RCM).

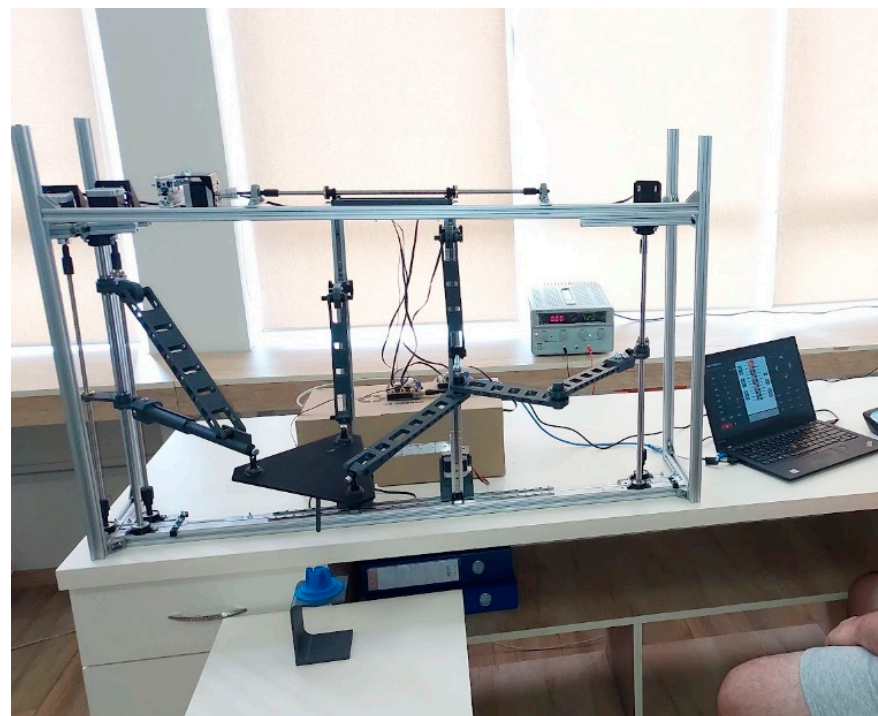


**Figure 19.** Experimental testing with the SILS mockup platform.

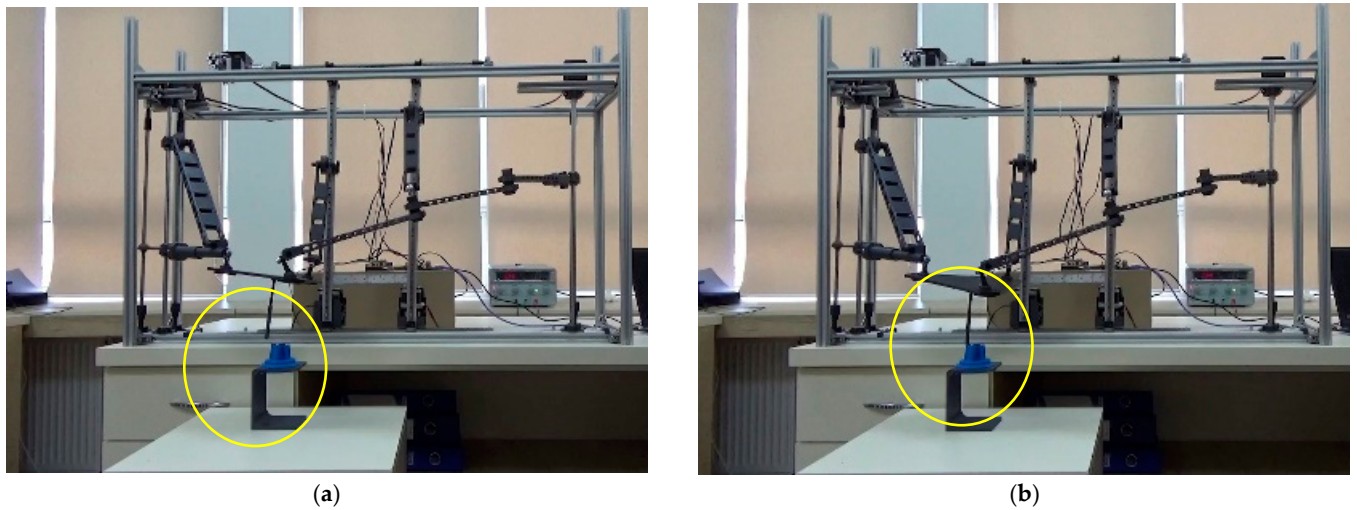


**Figure 20.** Experimental tests: the robot structure is performing movements with the mobile platform (to reach the RCM). (a) The laparoscope approaches the SILS port; (b) the tip of the laparoscope touches the SILS port.



**Figure 21.** Experimental tests: The robot structure is inserting the instrument mockup through the SILS port. (a) The tip of the laparoscope is in the inserting point; (b) The laparoscope is oriented.



**Figure 22.** Experimental tests: the robot structure is performing motions with the instrument inside the surgical field.

A sequence of images from the experimental testing of the robot is presented, pointing out each of the main operating stages of the parallel robot for SILS.

The use of the SpaceMouse as motion input for the positioning and control of the medical instruments is a promising solution, but for the actuation of dexterous instruments,

the control algorithm must be modified to use the linear motions for the actuation of the entire instrument and the rotational motions to control the orientation of the distal head.

Another experimental test implied an accuracy assessment of the robotic system in laboratory conditions. For this assessment, the OptiTrack Motion Capture system was used [39–41]. The motion tracking system uses several cameras and a set of markers attached to the moving object in study to optically evaluate its evolution during the motion. Figure 23 shows the marker's placement on the robotic structure. A total number of 8 optical markers were used: markers M1 to M6 were used to track the motion of the  $q_1$  to  $q_6$  active joint joints, marker E was used to track the motion of the tip of the laparoscope (end-effector), marker Frame was used for the reference frame and the calibration of the OptiTrack system was made using the CS-400 calibration tool which was further used to set the reference system during the motion tracking and was placed on the table in front of the robot. The setup of the tracking system, along with the markers consisted of four Prime 41 infrared cameras placed in the front of the robot in order to monitor every marker placed on the robot. In order to accurately place the motion markers a four-step calibration procedure was defined:

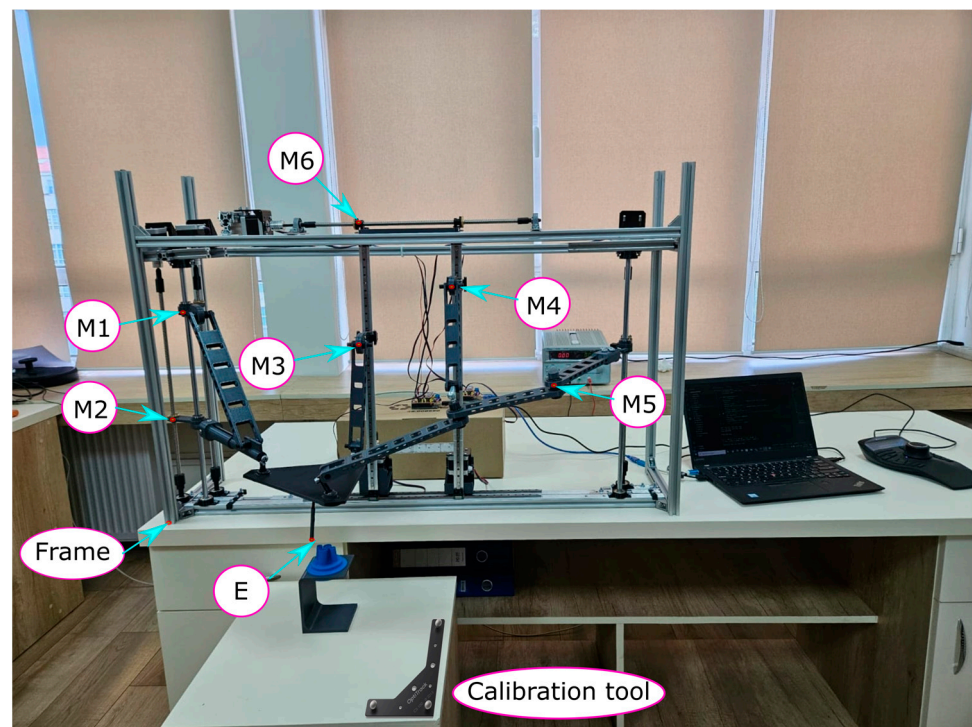


Figure 23. Optical markers placed on the robotic structure.

Step 1: Place the robotic system in the Home position where the orientation angles of the mobile platform are all equal to zero ( $\psi = \theta = \varphi = 0$ );

Step 2: Position as accurately as possible the markers on the robotic structure (the frame marker, the end-effector marker, and the active joints markers);

Step 3: Perform initial measurement with the motion tracking system and check the orientation angles, the position of the end-effector, and the active joints;

Step 4: If the measurements overlap with the mathematical model, then the calibration is successful; otherwise, the markers must be repositioned to fit as possible the measurements.

For consistency, the same trajectory numerically and graphically simulated in Section 5 was used. For this experimental run, there was no need for the Space Mouse because the trajectory of the end-effector was given as input in the control system of the robot. During the run, only the position parameters were monitored (no velocity and no acceleration). The results obtained during the optical motion tracking of the end-effector are presented

in Figure 24. In order to denoise the signal measured a Fast Fourier Transformation was applied to the recorded data.

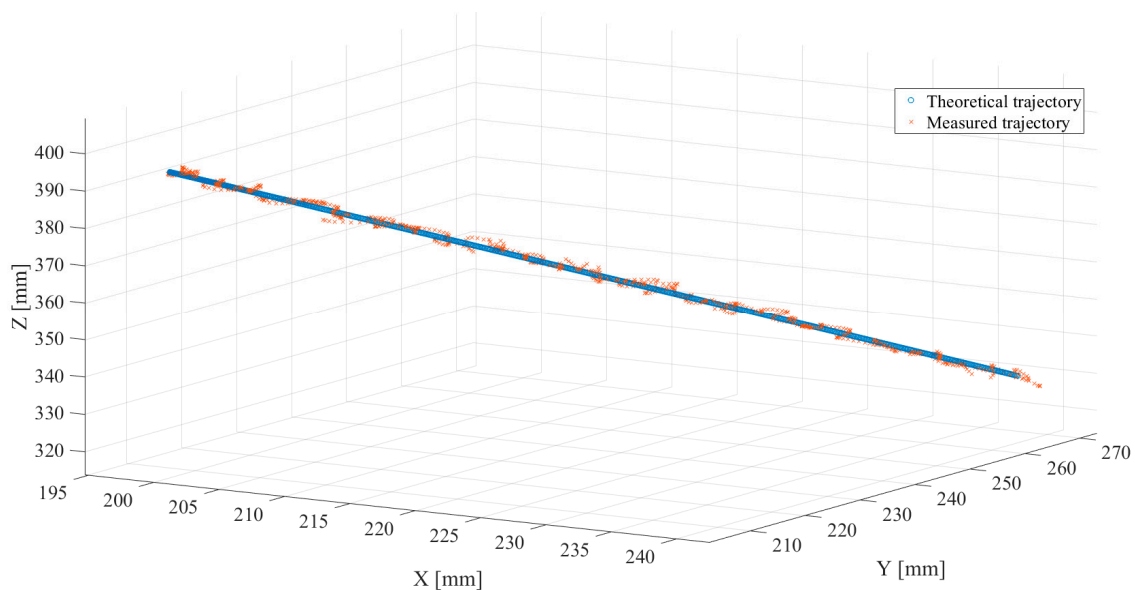


**Figure 24.** Results of theoretical simulation compared against the measured trajectory.

A total number of 10 measurements have been performed and the mean errors obtained for the end-effector coordinates and the active joints position are presented in Table 2. The mean positioning accuracy recorded at the level of the end-effector was  $2 \pm 0.5$  mm, an accuracy considered acceptable for the initial development of the robotic system. The main source of error during the optical measurements was considered to be caused by the optical tracking system accuracy and the light source within the room.

**Table 2.** Mean square error for the measured data using OptiTrack.

Coordinate	Mean Value	Coordinate	Mean Value
$X_E$	0.609 mm	$q_1$	-0.243 mm
$Y_E$	0.885 mm	$q_2$	-0.588 mm
$Z_E$	0.306 mm	$q_3$	-0.488 mm
$\psi$	3.430 deg	$q_4$	0.553 mm
$\theta$	1.255 deg	$q_5$	0.457 mm
$\varphi$	1.294 deg	$q_6$	-0.227 mm

## 7. Discussions

In this paper, the development of a parallel robot for SILS is presented. Starting from the medical protocol developed with the help of medical experts in minimally invasive procedures resulted in the requirements of the medical robot for SILS. Using Siemens NX as a modeling and simulation environment, the concept design of the robotic structure was developed and used to define the kinematics of the robotic structure. Following the kinematics computation of the robotic structure, the mathematically determined singularities were analyzed. No singularity resulted for the direct mathematical model, but for the inverse mathematical model resulted in a nine-term product of which several were eliminated because there were no vanishing conditions. For the terms that could not be eliminated, a numerical computation was performed in MATLAB to determine the problematic intervals where the terms were close to achieving zero value. These intervals were recorded for further implementation on the singularity avoidance module of the control system. To increase the rigidity of the robotic system, several components were analyzed using FEM. The simulation revealed several large displacements regarding some main components, so these components were redesigned. Although after the redesign the

displacements were still quite large, the rigidity request for the scale model was fulfilled, and a low-cost experimental model was further developed. A numerical and graphical simulation was performed and the results overlapped on the same graphical window in order to identify variations between the numerical model determined using MATLAB and the 3D model developed using Siemens NX. No differences were identified between the two simulations and the mathematical model of the robot was validated. The control system of the experimental model was developed using two Arduino boards to control the six motors required by the kinematics of the robotic structure. For functional validation purposes, a 3D mouse was used to replace the surgeon haptic device, the mouse being able to control the 6-DOF mobile platform of the robot. The functionality of the experimental model, hence of the kinematics of the 6-DOF SILS robotic system was validated using several motion scenarios similar to the medical procedure. Using optical tracking systems, the accuracy of the robotic system was determined to be  $2 \pm 0.5$  mm, an accuracy that is acceptable for the current state of the robot, but which may be improved with further development of the mechanisms.

## 8. Conclusions

The work presented within this paper describes several design stages of a parallel robot for potential use in SILS procedures. The current state of the development reveals a low-cost designed prototype, able to perform the motions required by the medical procedure in order to manipulate a mobile platform containing a laparoscopic camera, outside the body of the patient, to position the tip of the laparoscopic camera at the entry point in the trocar and then to insert the camera on a linear trajectory. After insertion, the motion of the laparoscope is constrained with respect to RCM determined by the trocar. The developed prototype represents the initial design of the robot, using low-cost materials and 3D-printed components, for this a positioning accuracy of  $2 \pm 0.5$  mm was determined. The accuracy obtained is not great but considering the development stage of the robotic system is allowable and it may be improved through the use of reliable components (accurately machined components, bearings, more resilient parts instead of 3D printed components) and the usability of the robotic system may be improved by using materials compatible with the hospital environment. Further work implies optimization of the experimental model and development of a friendly graphical user interface able to control the robotic system with respect to the medical procedure and the medical protocol.

**Author Contributions:** Conceptualization, P.T., C.V. and D.P.; data curation, C.R.; formal analysis, C.R.; investigation, N.A.H. and P.T.; methodology, B.G., T.A., P.T., C.V. and D.P.; resources, D.P.; software, B.G. and T.A.; supervision, N.A.H. and D.P.; validation, T.A., R.L. and C.V.; visualization, B.G.; writing—original draft, B.G., P.T., C.V. and D.P.; writing—review and editing, R.L. All authors have read and agreed to the published version of the manuscript.

**Funding:** This work was supported by the project New smart and adaptive robotics solutions for personalized minimally invasive surgery in cancer treatment—ATHENA, funded by European Union—NextGenerationEU and Romanian Government, under National Recovery and Resilience Plan for Romania, contract no. 760072/23.05.2023, code CF 116/15.11.2022, through the Romanian Ministry of Research, Innovation and Digitalization, within Component 9, investment I8 and a grant of the Ministry of Research, Innovation and Digitalization, CNCS/CCCDI—UEFISCDI, project number PCE171/2021—Challenge within PNCDI III

**Data Availability Statement:** <https://cester.utcluj.ro/Challenge/publications.html> (accessed on 12 September 2023).

**Conflicts of Interest:** The authors declare no conflict of interest.

## References

1. Schlich, T.; Tang, C.L. Patient choice and the history of minimally invasive surgery. *Lancet* **2016**, *388*, 1369–1370. [[CrossRef](#)]
2. Rao, P.; Rao, P.; Bhagwat, S. Single-incision laparoscopic surgery—Current status and controversies. *J. Minimal Access Surg.* **2011**, *7*, 6. [[CrossRef](#)]

3. Sugimoto, M.; Tanaka, K.; Matsuoka, Y.; Man-I, M.; Morita, Y.; Tanaka, S.; Fujiwara, S.; Azuma, T. da Vinci robotic single-incision cholecystectomy and hepatectomy using single-channel GelPort access. *J. Hepatobiliary Pancreat. Sci.* **2011**, *18*, 493–498. [[CrossRef](#)] [[PubMed](#)]
4. Sharma, A.; Dahiya, P.; Khullar, R.; Soni, V.; Baijal, M.; Chowbey, P.K. Single-Incision Laparoscopic Surgery (SILS) in Biliary and Pancreatic Diseases. *Indian J. Surg.* **2012**, *74*, 13–21. [[CrossRef](#)]
5. Fagenson, A.M.; Gleeson, E.M.; Pitt, H.A.; Lau, K.N. Minimally Invasive Hepatectomy in North America: Laparoscopic Versus Robotic. *J. Gastrointest. Surg.* **2021**, *25*, 85–93. [[CrossRef](#)]
6. De Pastena, M.; Esposito, A.; Paiella, S.; Surci, N.; Montagnini, G.; Marchegiani, G.; Malleo, G.; Secchetin, E.; Casetti, L.; Ricci, C.; et al. Cost-effectiveness and quality of life analysis of laparoscopic and robotic distal pancreatectomy: A propensity score-matched study. *Surg. Endosc.* **2021**, *35*, 1420–1428. [[CrossRef](#)] [[PubMed](#)]
7. de Groot, E.M.; Goense, L.; Ruurda, J.P.; van Hillegersberg, R. State of the art in esophagectomy: Robotic assistance in the abdominal phase. *Updat. Surg.* **2021**, *73*, 823–830. [[CrossRef](#)]
8. Boga, M.S.; Sönmez, M.G.; Karamık, K.; Özsoy, Ç.; Aydın, A.; Savas, M.; Ateş, M. Long-term outcomes of minimally invasive surgeries in partial nephrectomy. Robot or laparoscopy? *Int. J. Clin. Pract.* **2021**, *75*, e13757. [[CrossRef](#)] [[PubMed](#)]
9. Barajas-Gamboa, J.S.; Huidobro, F.; Jensen, J.; Luengas, R.; Rodriguez, J.; Abril, C.; Corcelles, R.; Kroh, M. First in-human experience with a novel robotic platform and Magnetic Surgery System. *Int. J. Med. Robot. Comput. Assist. Surg.* **2021**, *17*, 1–7. [[CrossRef](#)] [[PubMed](#)]
10. Aiolfi, A.; Lombardo, F.; Bonitta, G.; Danelli, P.; Bona, D. Systematic review and updated network meta-analysis comparing open, laparoscopic, and robotic pancreaticoduodenectomy. *Updat. Surg.* **2021**, *73*, 909–922. [[CrossRef](#)]
11. Kanji, F.; Catchpole, K.; Choi, E.; Alfred, M.; Cohen, K.; Shouhed, D.; Anger, J.; Cohen, T. Work-system interventions in robotic-assisted surgery: A systematic review exploring the gap between challenges and solutions. *Surg. Endosc.* **2021**, *35*, 1976–1989. [[CrossRef](#)]
12. Kim, K.H.; Song, W.; Yoon, H.; Lee, D.H. Single-port robot-assisted radical prostatectomy with the da Vinci SP system: A single surgeon's experience. *Investig. Clin. Urol.* **2020**, *61*, 173–179. [[CrossRef](#)]
13. Armijo, P.R.; Pagkratis, S.; Boilesen, E.; Tanner, T.; Oleynikov, D. Growth in robotic-assisted procedures is from conversion of laparoscopic procedures and not from open surgeons' conversion: A study of trends and costs. *Surg. Endosc.* **2018**, *32*, 2106–2113. [[CrossRef](#)]
14. Konietzschke, R.; Hagn, U.; Nickl, M.; Jorg, S.; Tobergte, A.; Passig, G.; Seibold, U.; Le-Tien, L.; Kubler, B.; Groger, M.; et al. The DLR MiroSurge—A robotic system for surgery. In Proceedings of the 2009 IEEE International Conference on Robotics and Automation, Kobe, Japan, 12–17 May 2009; pp. 1589–1590. [[CrossRef](#)]
15. McCarus, S.D. Senhance Robotic Platform System for Gynecological Surgery. *JSLs J. Soc. Laparosc. Robot. Surg.* **2021**, *25*, e2020-00075. [[CrossRef](#)] [[PubMed](#)]
16. Jang, E.J.; Kang, S.H.; Kim, K.W. Early Outcomes of Robotic Single Site Cholecystectomy Using the DaVinci Xi<sup>®</sup> System. *JSLs J. Soc. Laparosc. Robot. Surg.* **2021**, *25*, e2020-00082. [[CrossRef](#)]
17. Pisla, D.; Calin, V.; Birlescu, I.; Al Hajjar, N.; Gherman, B.; Radu, C.; Plitea, N. Risk Management for the Reliability of Robotic Assisted Treatment of Non-resectable Liver Tumors. *Appl. Sci.* **2019**, *10*, 52. [[CrossRef](#)]
18. Pisla, D.; Tarnita, D.; Tucan, P.; Tohanean, N.; Vaida, C.; Geonea, I.D.; Bogdan, G.; Abrudan, C.; Carbone, G.; Plitea, N. A Parallel Robot with Torque Monitoring for Brachial Monoparesis Rehabilitation Tasks. *Appl. Sci.* **2021**, *11*, 9932. [[CrossRef](#)]
19. Kojcev, R.; Fuerst, B.; Zettinig, O.; Fotouhi, J.; Lee, S.C.; Frisch, B.; Taylor, R.; Sinibaldi, E.; Navab, N. Dual-robot ultrasound-guided needle placement: Closing the planning-imaging-action loop. *Int. J. Comput. Assist. Radiol. Surg.* **2016**, *11*, 1173–1181. [[CrossRef](#)]
20. Taylor, R.H.; Kazanzides, P. Medical Robotics and Computer-Integrated Interventional Medicine. In *Biomedical Information Technology*; Feng, D., Ed.; Elsevier: Amsterdam, The Netherlands, 2008; pp. 393–416. [[CrossRef](#)]
21. Taylor, R.; Stoianovici, D. Medical robotics in computer-integrated surgery. *IEEE Trans. Robot. Autom.* **2003**, *19*, 765–781. [[CrossRef](#)]
22. Special Section: Mechanisms and Robots for Safe Human–Robot Physical Interaction. *J. Mech. Robot.* **2019**, *11*, 1–2. [[CrossRef](#)]
23. Simaan, N.; Taylor, R.H.; Choset, H. Intelligent Surgical Robots with Situational Awareness. *Mech. Eng.* **2015**, *137*, S3–S6. [[CrossRef](#)]
24. Simaan, N.; Taylor, R.; Flint, P. A dexterous system for laryngeal surgery. In Proceedings of the IEEE International Conference on Robotics and Automation, 2004 Proceedings, ICRA '04, 2004, New Orleans, LA, USA, 26 April–1 May 2004; Volume 1, pp. 351–357. [[CrossRef](#)]
25. Dario, P. Editorial Medical Robotics and Bionics: A New Interdisciplinary Adventure. *IEEE Trans. Med. Robot. Bionics* **2019**, *1*, 1–3. [[CrossRef](#)]
26. Dario, P.; Menciassi, A. Robot Pills. *Sci. Am.* **2010**, *303*, 62–65. [[CrossRef](#)] [[PubMed](#)]
27. Dario, P.; Ciarletta, P.; Menciassi, A.; Kim, B. Modeling and Experimental Validation of the Locomotion of Endoscopic Robots in the Colon. *Int. J. Robot. Res.* **2004**, *23*, 549–556. [[CrossRef](#)]
28. Wei, H.; Li, K.; Xu, D.; Tan, W. Design of a Laparoscopic Robot System Based on Spherical Magnetic Field. *Appl. Sci.* **2019**, *9*, 2070. [[CrossRef](#)]
29. Tian, H.; Zheng, C.; Jiang, J.; Li, J.; Li, Y.; Yao, Y. Design, Kinematic, Dynamic, and Stiffness Analysis of A 5-DOF Single-Incision Laparoscopic Surgery Robot. *Int. J. Robot. Mechatron.* **2020**, *7*, 1–16.

30. Pisla, D.; Crisan, N.; Ulinici, I.; Gherman, B.; Radu, C.; Tucan, P.; Vaida, C. Structural Study of a Robotic System for Sils Surgery. In *International Workshop on Medical and Service Robots*; Springer Nature: Cham, Switzerland, 2023; pp. 20–31. [\[CrossRef\]](#)
31. FAtug, F.; Burgess, S.V.; Ruiz-Deya, G.; Mendes-Torres, F.; Castle, E.P.; Thomas, R. Long-term durability of laparoscopic decortication of symptomatic renal cysts. *Urology* **2006**, *68*, 272–275. [\[CrossRef\]](#)
32. Kowalewski, K.F.; Seifert, L.; Ali, S.; Schmidt, M.W.; Seide, S.; Haney, C.; Tapking, C.; Shamiyeh, A.; Kulu, Y.; Hackert, T.; et al. Functional outcomes after laparoscopic versus robotic-assisted rectal resection: A systematic review and meta-analysis. *Surg. Endosc.* **2021**, *35*, 81–95. [\[CrossRef\]](#)
33. Yang, Y.; Liu, H.; Zheng, H.; Peng, Y.; Yu, Y. Two types of remote-center-of-motion deployable manipulators with dual scissor-like mechanisms. *Mech. Mach. Theory* **2021**, *160*, 104274. [\[CrossRef\]](#)
34. Li, B.; Li, Y.; Zhao, X. Kinematics analysis of a novel over-constrained three degree-of-freedom spatial parallel manipulator. *Mech. Mach. Theory* **2016**, *104*, 222–233. [\[CrossRef\]](#)
35. Lu, S.; Li, Y.; Ding, B. Kinematics and dynamics analysis of the 3PUS-PRU parallel mechanism module designed for a novel 6-DOF gantry hybrid machine tool. *J. Mech. Sci. Technol.* **2020**, *34*, 345–357. [\[CrossRef\]](#)
36. Gosselin, C. Determination of the Workspace of 6-DOF Parallel Manipulators. *J. Mech. Des.* **1990**, *112*, 331–336. [\[CrossRef\]](#)
37. Merlet, J.-P.; Gosselin, C.M.; Mouly, N. Workspaces of planar parallel manipulators. *Mech. Mach. Theory* **1998**, *33*, 7–20. [\[CrossRef\]](#)
38. Merlet, J.-P. *Parallel Robots*, 2nd ed.; Springer: Berlin/Heidelberg, Germany, 2000.
39. Chen, Q.; Zhou, Y.; Wang, Y.; Zhu, M.; Guo, L.; He, C. Research on stability and accuracy of the OptiTrack system based on mean error. In *International Symposium on Artificial Intelligence and Robotics 2021*; Nakashima, S., Mu, S., Lu, H., Eds.; SPIE: Bellingham, WA, USA, 2021; p. 75. [\[CrossRef\]](#)
40. Ameler, T.; Warzecha, M.; Hes, D.; Fromke, J.; Schmitz-Stolbrink, A.; Friedrich, C.M.; Blohme, K.; Brandt, L.; Brungel, R.; Hensel, A.; et al. A Comparative Evaluation of SteamVR Tracking and the OptiTrack System for Medical Device Tracking. In *Proceedings of the 2019 41st Annual International Conference of the IEEE Engineering in Medicine and Biology Society (EMBC)*, Berlin, Germany, 23–27 July 2019; pp. 1465–1470. [\[CrossRef\]](#)
41. Dena Ruiz, J.A.; Aouf, N. Real-Time Setup with PD and Backstepping Control for a Pelican Quadrotor. In *Proceedings of the 14th International Conference on Informatics in Control, Automation and Robotics*, Madrid, Spain, 26–28 July 2017; pp. 676–681. [\[CrossRef\]](#)

**Disclaimer/Publisher’s Note:** The statements, opinions and data contained in all publications are solely those of the individual author(s) and contributor(s) and not of MDPI and/or the editor(s). MDPI and/or the editor(s) disclaim responsibility for any injury to people or property resulting from any ideas, methods, instructions or products referred to in the content.